

Mass profiles and $c - M_{\text{DM}}$ relation in X-ray luminous galaxy clusters

S. Ettori^{1,2}, F. Gastaldello^{3,5,6}, A. Leccardi^{3,4}, S. Molendi³, M. Rossetti³, D. Buote⁵, and M. Meneghetti^{1,2}

¹ INAF, Osservatorio Astronomico di Bologna, via Ranzani 1, I-40127 Bologna, Italy

² INFN, Sezione di Bologna, viale Berti Pichat 6/2, I-40127 Bologna, Italy

³ INAF, IASF, via Bassini 15, I-20133 Milano, Italy

⁴ Università degli Studi di Milano, Dip. di Fisica, via Celoria 16, I-20133 Milano, Italy

⁵ Department of Physics and Astronomy, University of California, Irvine, CA 92697-4575

⁶ Occhialini Fellow

Received 24 June 2010 / Accepted 14 September 2010

ABSTRACT

Context. Galaxy clusters represent valuable cosmological probes using tests that mainly rely on measurements of cluster masses and baryon fractions. X-ray observations represent one of the main tools for uncovering these quantities.

Aims. We aim to constrain the cosmological parameters Ω_m and σ_8 using the observed distribution of the both values of the concentrations and dark mass within R_{200} and of the gas mass fraction within R_{500} .

Methods. We applied two different techniques to recover the profiles the gas and dark mass, described according to the Navarro, Frenk & White (1997, ApJ, 490, 493) functional form, of a sample of 44 X-ray luminous galaxy clusters observed with *XMM-Newton* in the redshift range 0.1 – 0.3. We made use of the spatially resolved spectroscopic data and of the PSF–deconvolved surface brightness and assumed that hydrostatic equilibrium holds between the intracluster medium and the gravitational potential. We evaluated several systematic uncertainties that affect our reconstruction of the X-ray masses.

Results. We measured the concentration c_{200} , the dark mass M_{200} and the gas mass fraction in all the objects of our sample, providing the largest dataset of mass parameters for galaxy clusters in the redshift range 0.1 – 0.3. We confirm that a tight correlation between c_{200} and M_{200} is present and in good agreement with the predictions from numerical simulations and previous observations. When we consider a subsample of relaxed clusters that host a low entropy core, we measure a flatter $c - M$ relation with a total scatter that is lower by 40 per cent. We conclude, however, that the slope of the $c - M$ relation cannot be reliably determined from the fitting over a narrow mass range as the one considered in the present work. From the distribution of the estimates of c_{200} and M_{200} , with associated statistical (15–25%) and systematic (5–15%) errors, we used the predicted values from semi-analytic prescriptions calibrated through N-body numerical runs and obtain $\sigma_8 \Omega_m^{0.60 \pm 0.03} = 0.45 \pm 0.01$ (at 2σ level, statistical only) for the subsample of the clusters where the mass reconstruction has been obtained more robustly and $\sigma_8 \Omega_m^{0.56 \pm 0.04} = 0.39 \pm 0.02$ for the subsample of the 11 more relaxed LEC objects. With the further constraint from the gas mass fraction distribution in our sample, we break the degeneracy in the $\sigma_8 - \Omega_m$ plane and obtain the best-fit values $\sigma_8 \approx 1.0 \pm 0.2$ (0.83 ± 0.1 when the subsample of the more relaxed objects is considered) and $\Omega_m = 0.26 \pm 0.02$.

Conclusions. We demonstrate that the analysis of the distribution of the $c_{200} - M_{200} - f_{\text{gas}}$ values represents a mature and competitive technique in the present era of precision cosmology, even though it needs more detailed analysis of the output of larger sets of cosmological numerical simulations to provide definitive and robust results.

Key words. galaxies: cluster: general – intergalactic medium – X-ray: galaxies – cosmology: observations – dark matter.

1. Introduction

The distribution of the total and baryonic mass in galaxy clusters is a fundamental ingredient to validate the scenario of structure formation in a Cold Dark Matter (CDM) Universe. Within this scenario, the massive virialized objects are powerful cosmological tools able to constrain the fundamental parameters of a given CDM model. The N -body simulations of structure formation in CDM models indicate that dark matter halos aggregate with a typical mass density profile characterized by only 2 parameters, the concentration c and the scale radius r_s (e.g. Navarro et al. 1997, hereafter NFW). The product of these two quantities fixes the radius within which the mean cluster density is 200 times the critical value at the cluster’s redshift [i.e.

$R_{200} = c_{200} \times r_s$ and the cluster’s volume $V = 4/3\pi R_{200}^3$ is equal to $M_{200}/(200\rho_{c,z})$, where M_{200} is the cluster gravitating mass within R_{200}]. With this prescription, the structural properties of DM halos from galaxies to galaxy clusters are dependent on the halo mass, with systems at higher masses less concentrated. Moreover, the concentration depends upon the assembly redshift (e.g. Bullock et al. 2001, Wechsler et al. 2002, Zhao et al. 2003, Li et al. 2007), which happens to be later in cosmologies with lower matter density, Ω_m , and lower normalization of the linear power spectrum on scale of $8h^{-1}$ Mpc, σ_8 , implying less concentrated DM halos of given mass. The concentration – mass relation, and its evolution in redshift, is therefore a strong prediction obtained from CDM simulations of structure formation and is quite sensitive to the assumed cosmological parameters (NFW; Bullock et al. 2001; Eke, Navarro & Steinmetz 2001; Dolag et al. 2004; Neto et al. 2007; Macciò et al. 2008). In this context, NFW, Bullock et al. 2001 (with revision after Macciò et

Send offprint requests to: S. Ettori

Correspondence to: stefano.ettori@oabo.inaf.it

al. 2008) and Eke et al. 2001 have provided simple and powerful models that match the predictions from numerical simulations and allow comparison with the observational measurements.

Recent X-ray studies (Pointecouteau, Arnaud & Pratt 2005; Vikhlinin et al. 2006; Voigt & Fabian 2006; Zhang et al. 2006; Buote et al. 2007) have shown good agreement between observational constraints at low redshift and theoretical expectations. By fitting 39 systems in the mass range between early-type galaxies up to massive galaxy clusters, Buote et al. (2007) confirm with high significance that the concentration decreases with increasing mass, as predicted from CDM models, and require a σ_8 , the dispersion of the mass fluctuation within spheres of comoving radius of $8 h^{-1}$ Mpc, in the range $0.76 - 1.07$ (99% confidence) definitely in contrast to the lower constraints obtained, for instance, from the analysis of the *WMAP* 3 years data. Since it is based upon a selection of the most relaxed systems, these results assumed a 10% upward early formation bias in the concentration parameter for relaxed halos. Using a sample of 34 massive, dynamically relaxed galaxy clusters resolved with *Chandra* in the redshift range $0.06 - 0.7$, Schmidt & Allen (2007) highlight a possible tension between the observational constraints and the numerical predictions, in the sense that either the relation is steeper than previously expected or some redshift evolution has to be considered. Comerford & Natarajan (2007) compiled a large dataset of observed cluster concentration and masses, finding a normalization higher by at least 20 per cent than the results from simulations. In the sample, they use also strong lensing measurements of the concentration concluding that these are systematically larger than the ones estimated in the X-ray band, and 55 per cent higher, on average, than the rest of the cluster population. Recently, Wojtak & Łokas (2010) analyze kinematic data of 41 nearby ($z < 0.1$) relaxed objects and find a normalization of the concentration – mass relation fully consistent with the amplitude of the power spectrum σ_8 estimated from *WMAP1* data and within 1σ from the constraint obtained from *WMAP5*.

In this work, we use the results of the spectral analysis presented in Leccardi & Molendi (2008) for a sample of 44 X-ray luminous galaxy clusters located in the redshift range $0.1 - 0.3$ with the aim to (1) recover their total and gas mass profiles, (2) constraining the cosmological parameters σ_8 and Ω_m through the analysis of the measured distribution of c_{200} , M_{200} and baryonic mass fraction in the mass range above $10^{14} M_{\odot}$. We note that this is the statistically largest sample for which this study has been carried on up to now between $z = 0.1$ and $z = 0.3$.

The outline of our work is the following. In Section 2, we describe the dataset of *XMM-Newton* observations used in our analysis to recover the gas and total mass profiles with the techniques presented in Section 3. In Section 4, we present a detailed discussion of the main systematic uncertainties that affect our measurements. We investigate the $c_{200} - M_{200}$ relation in Section 5. By using our measurements of c_{200} and M_{200} , we constrain the cosmological parameters σ_8 and Ω_m , breaking the degeneracy between these parameters by adding the further cosmological constraints from our estimates of the cluster baryon fraction, as discussed in Section 6. We summarize our results and draw the conclusion of the present study in Section 7. Throughout this work, if not otherwise stated, we plot and tabulate values estimated by assuming a Hubble constant $H_0 = 70 h_{70}^{-1} \text{ km s}^{-1} \text{ Mpc}^{-1}$ and $\Omega_m = 1 - \Omega_{\Lambda} = 0.3$, and quote errors at the 68.3 per cent (1σ) level of confidence.

We list here in alphabetic order, with the adopted acronyms, the work to which we will refer more often in the present study: Bullock et al. (2001 – B01); Dolag et al. (2004 – D04); Eke, Navarro & Steinmetz (2001 – E01); Leccardi & Molendi (2008

– LM08); Macciò et al. (2008 – M08); Navarro, Frenk & White (1997 – NFW); Neto et al. (2007 – N07).

2. The dataset

Leccardi & Molendi (2008) have retrieved from the *XMM-Newton* archive all observations of clusters available at the end of May 2007 (and performed before March 2005, when the CCD6 of EPIC-MOS1 was switched off) and satisfying the selection criteria to be hot ($kT > 3.3$ keV), at intermediate redshift ($0.1 < z < 0.3$), and at high galactic latitude ($|b| > 20^\circ$). Upper and lower limits to the redshift range are determined, respectively, by the cosmological dimming effect and the size of the EPIC field of view ($15'$ radius). Out of 86 observations, 23 were excluded because they are highly affected by soft proton flares (see Table 1 in LM08) and have cleaned exposure time less than 16 ks when summing MOS1 and MOS2. Furthermore, 15 observations were excluded because they show evidence of recent and strong interactions (see Table 2 in LM08). The spectral analysis of the remaining 48 exposures, for a total of 44 clusters, is presented in LM08 and summarized in the next subsection. In Table 1, we present the list of the clusters analyzed in the present work.

2.1. Spatially resolved spectral analysis

We use gas temperature profiles measured by LM08. A detailed description of how the profiles were obtained and tested against systematic uncertainties can be found in their paper. Here we briefly review some of the most important points. Unlike most temperature estimates the one reported in LM08 have been secured by performing background modelling rather than background subtraction. Great care and considerable effort has gone into building an accurate model of the EPIC background, both in terms of its instrumental and cosmic components. Unfortunately the impossibility of performing an adequate monitoring of the *pn* instrumental background during source observation resulted in the exclusion of this detector from the analysis. Therefore, we adopt the measurements obtained from the two MOS instruments (M1 and M2, hereafter) independently in the following analysis.

The impact of small errors in the background estimates on temperature and normalization estimates was tested both by performing Monte-Carlo simulations (a-priori tests) and by checking how results varied for different choices of key parameters (a-posteriori tests). The detailed analysis allowed to track systematic errors and provide an error budget including both statistical and systematic uncertainties.

The two profiles have been analyzed both independently and after they were combined as described below. M1 and M2 are cross-calibrated to about 5% (Mateos et al 2009). The largest discrepancy appears to be in the high energy range (above 4.5 keV), leading to a general tendency where M2 returns slightly softer spectra than M1. Since a similar comparison between M2 and *pn* shows that the latter returns even softer spectra, the M2 experiment may be viewed as returning spectra which are intermediate between M1 and *pn* in the $0.7 - 10$ keV band. As consequence of that, a systematic shift between the M1 and M2 temperature profiles is present, meaning that an higher measurements is obtained with M1. This shift is not very sensitive to the value of the temperature, but instead manifests itself as a difference between M1 and M2 in the shape of the radial temperature profile. Using as reference the value of gas temperature measured with M2, we estimate the median deviation in the different radial bins to be

Table 1. Sample of the galaxy clusters.

Cluster	Other name	z	Core Cl.	Entropy Cl.	X-ray refs.
RXCJ0003.8+0203	Abell2700	0.092	ICC	MEC	Pr07, Cr08
Abell3911	–	0.097	NCC	HEC	Sn08
Abell3827	–	0.098	ICC	MEC	Sn08
RXCJ0049.4-2931	AbellS0084	0.108	ICC	MEC	Si09
Abell2034	–	0.113	NCC	HEC	Ke03, Ba07
RXCJ1516.5-0056	Abell2051	0.115	NCC	HEC	Pr07, Cr08
RXCJ2149.1-3041	Abell3814	0.118	CC	LEC	Cr08, Le08
RXCJ1516.3+0005	Abell2050	0.118	NCC	HEC	Pr07, Cr08
RXCJ1141.4-1216	Abell1348	0.119	CC	LEC	Pr07, Cr08
RXCJ1044.5-0704	Abell1084	0.132	CC	LEC	Pr07, Cr08
Abell1068	RXCJ1040.7+3956	0.138	CC	LEC	Wi04, Sn08
RXCJ2218.6-3853	Abell3856	0.138	NCC	MEC	Pr07, Cr08
RXCJ0605.8-3518	Abell3378	0.141	CC	LEC	Pr07, Cr08, Sn08
RXCJ0020.7-2542	Abell22	0.142	NCC	HEC	Pr07, Cr08
Abell1413	RXCJ1155.3+2324	0.143	ICC	MEC	Vi05, Ba07, Sn08, Ca09
RXCJ2048.1-1750	Abell2328	0.147	NCC	HEC	Pr07, Cr08
RXCJ0547.6-3152	Abell3364	0.148	NCC	HEC	Pr07, Cr08
Abell2204	RXC J1632.7+0534	0.152	CC	LEC	Mo07, Sa09
RXCJ0958.3-1103	Abell907	0.153	CC	LEC	Vi05, Cr08
RXCJ2234.5-3744	Abell3888	0.153	NCC	HEC	Cr08
RXCJ2014.8-2430	RXCJ2014.8-24	0.161	CC	LEC	Cr08
RXCJ0645.4-5413	Abell3404	0.167	ICC	MEC	Cr08
Abell2218	–	0.176	NCC	HEC	Go04, Ba07
Abell1689	–	0.183	ICC	MEC	Pe98, An04, Ca09
Abell383	–	0.187	CC	LEC	Vi05, Ca09, Zh10
Abell209	–	0.206	NCC	MEC	Ca09
Abell963	–	0.206	ICC	MEC	Sm05, Ba07, Ca09
Abell773	–	0.217	NCC	HEC	Go04, Mo07, Ca09
Abell1763	–	0.223	NCC	HEC	Du08, Ca09
Abell2390	–	0.228	CC	LEC	Vi05, Mo07, Ca09, Zh10
Abell2667	–	0.230	CC	LEC	Ca09
RXCJ2129.6+0005	–	0.235	CC	LEC	Ca09, Zh10
Abell1835	–	0.253	CC	LEC	Mo07, Zh10
RXCJ0307.0-2840	Abell3088	0.253	CC	LEC	Fi05, Zh06
Abell68	–	0.255	NCC	HEC	Zh10
E1455+2232	RXCJ1457.2+2220	0.258	CC	LEC	Sn08
RXCJ2337.6+0016	–	0.273	NCC	HEC	Fi05, Zh06, Zh10
RXCJ0303.8-7752	–	0.274	NCC	HEC	Zh06
RXCJ0532.9-3701	–	0.275	CC ?	MEC	Fi05, Zh06
RXCJ0232.2-4420	–	0.284	Cool core remnant ?	MEC	Fi05, Zh06
ZW3146	RBS0864	0.291	CC	LEC	Mo07
RXCJ0043.4-2037	Abell2813	0.292	NCC	HEC	Zh06
RXCJ0516.7-5430	AbellS0520	0.295	NCC	HEC	Zh06
RXCJ1131.9-1955	Abell1300	0.307	NCC	HEC	Fi05, Zh06

Notes. We quote the name of the object, the redshift adopted and the classification based on their X-ray properties.

(*Core Cl.*): cool cores (CC), intermediate systems (ICC) and non-cool cores (NCC).

(*Entropy Cl.*): as in Leccardi et al. (2010), low (LEC), medium (MEC) and high (HEC) entropy cores characterizing clusters with stronger cooling cores and more relaxed structure (LEC), more disturbed objects (HEC) and systems with intermediate properties (MEC).

(*X-ray refs.*): Baldi et al. (2007, Ba07); Cavagnolo et al. (2009, Ca09); Croston et al. (2008, Cr08); Finoguenov et al. (2005, Fi05); Govoni et al. (2004, Go04); Kempner et al. (2003, Ke03); Morandi et al. (2007, Mo07); Pratt et al. (2007, Pr07); Sanderson et al. (2009, Sa09); Sivanandam et al. (2009, Si09); Snowden et al. (2008, Sn08); Vikhlinin et al. (2005, Vi05); Wise et al. (2004, Wi04); Zhang et al. (2006, Zh06); Zhang et al. (2010, Zh10).

4.8 % in the inner bin, 8.9 % in the following 4 bins, 10 % from the 5th bin upwards. The two profiles are then combined by a weighted mean and a further systematic error is added, as described in Leccardi & Molendi (2008; see Section 5.3): i.e. 2, 3 and 5 per cent increases are considered at $0.3 < r/R_{180} < 0.36$,

$0.36 < r/R_{180} < 0.45$ and $r/R_{180} > 0.45$, respectively. For this purpose, R_{180} as defined in Tab. 3 in Leccardi & Molendi (2008) is considered. An error of the same amount is propagated in quadrature with the statistical error.

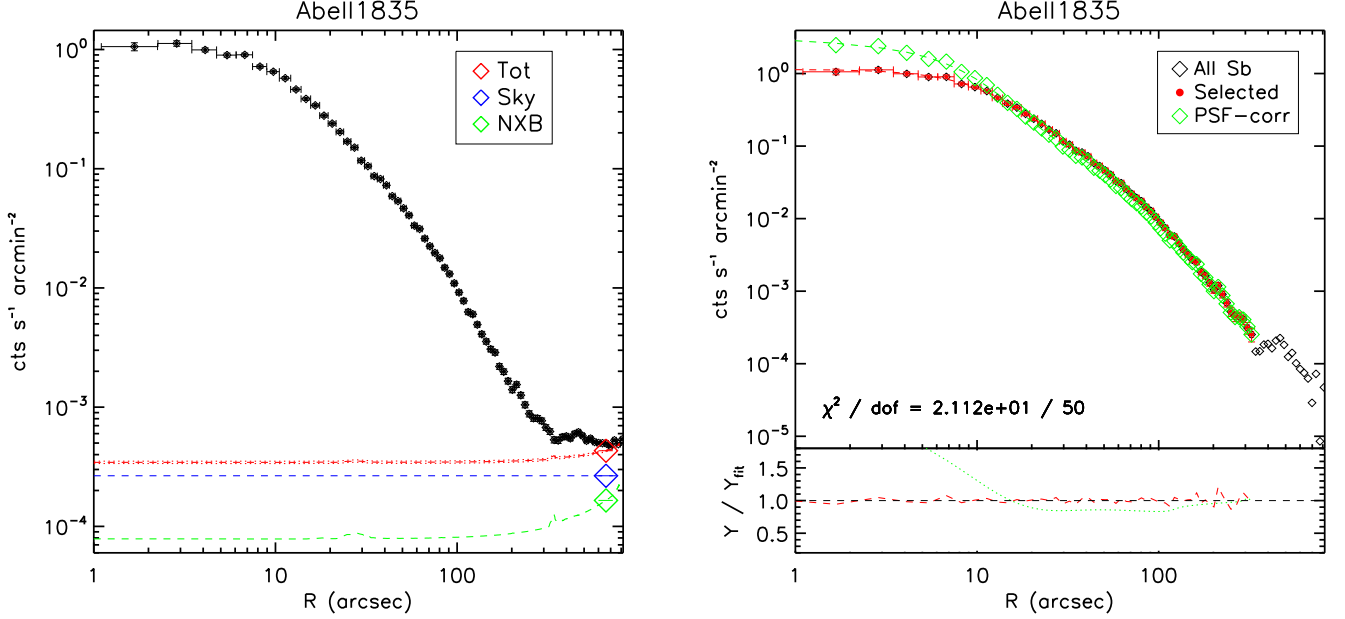


Fig. 1. (*Left*) Surface brightness profile in the 0.7 – 1.2 keV band (black filled circles) of Abell1835 compared with the profiles of the background components. The open diamonds show the count rate predicted from the background spectral model in the annulus 10–12 arcmin and rescaled for the mean vignetting correction of 0.472 at those radii: the instrumental component (NXB; green), the photon component (CXB + galactic foregrounds; blue) and the total background (sky + instrumental; red). The dashed lines show the background profiles that we have used in our analysis: the “photon” background (blue), which is constant and corresponds to the value in the outer annulus rescaled to the center, and the instrumental background profile (green), increasing with radius in order to consider the over-correction of this component. The red dashed line shows the total background that we have subtracted from our source plus background profile, with its associated 1σ statistical error (red dotted lines) obtained with a Monte Carlo simulation. Note that the intensity of the background components and their relative contribution vary significantly from cluster to cluster. (*Right*) Example of the PSF-corrected background-subtracted surface brightness profile as obtained after the analysis outlined in Sect. 2.2. This example refers to Abell1835, one of the objects with the largest smearing effect due to the combination of the telescope’s PSF and the centrally peaked intrinsic profile.

On the other hand, no significant effect is noticed when the values of the normalization of the thermal model K obtained from the two different instruments are compared. The combined profile is then the direct result of the weighted mean of the two estimates.

Unlike in LM08, where the focus was on the measure of the T_{gas} profile in outer regions, here we need to recover a detailed description of both the T_{gas} and surface brightness S_{b} profiles at large and small radii. A significant improvement compared to the treatment by LM08 has been the correction of the spectral mixing between different annuli caused by the finite PSF of the MOS instruments. We adopted the cross-talk modification of the ancillary region file (ARF) generation software (using the *crossregionarf* parameter of the *argen* task of SAS), treating the cross-talk contribution to the spectrum of a given annulus from a nearby annulus as an additional model component (see Snowden et al. 2008). This is a thermal model with parameters linked to the thermal spectrum fitted to the nearby annulus and associated to the appropriate ARF file of that region (i.e., the usual ARF familiar to X-ray astronomers). We found the correction to be important in particular to the first two annuli used in the analysis. The annuli have been therefore fitted jointly in XSPEC version 12 (Arnaud 1996), which allows to associate different models to different RMF and ARF files. A comparison of the values obtained with this modelling and the values quoted in

Snowden et al. (2008) for the 16 clusters in common with our sample give results in agreement within the errors.

2.2. Analysis of the surface brightness profile

We extend the spectral analysis presented in LM08 with a spatial analysis of the combined exposure-corrected M1-M2 images.

We extract surface brightness profiles from MOS images in the energy band 0.7 – 1.2 keV, in order to keep the background as low as possible with respect to the source. For this reason, we avoid the intense fluorescent instrumental lines of Al (~ 1.5 keV) and Si (~ 1.8 keV) (LM08). To correct for the vignetting, we divide the images by the corresponding exposure maps. From the surface brightness profiles, we subtract the background that is estimated starting from the spectral modelling of the background components in the external ring 10–12 arcmin (see LM08 for details on the adopted models). We recall here that in the procedure of LM08 the normalizations of the background components are the only free parameters of the fit and that the galactic foreground emission, the cosmic X-ray background and the cosmic ray induced continuum give a significant contribution in the 0.7 – 1.2 keV energy range. The intensities of the background components in the annulus 10–12 arcmin are given by the count rates predicted by the best fit spectral model in this region. In order to associate errors to these count rates,

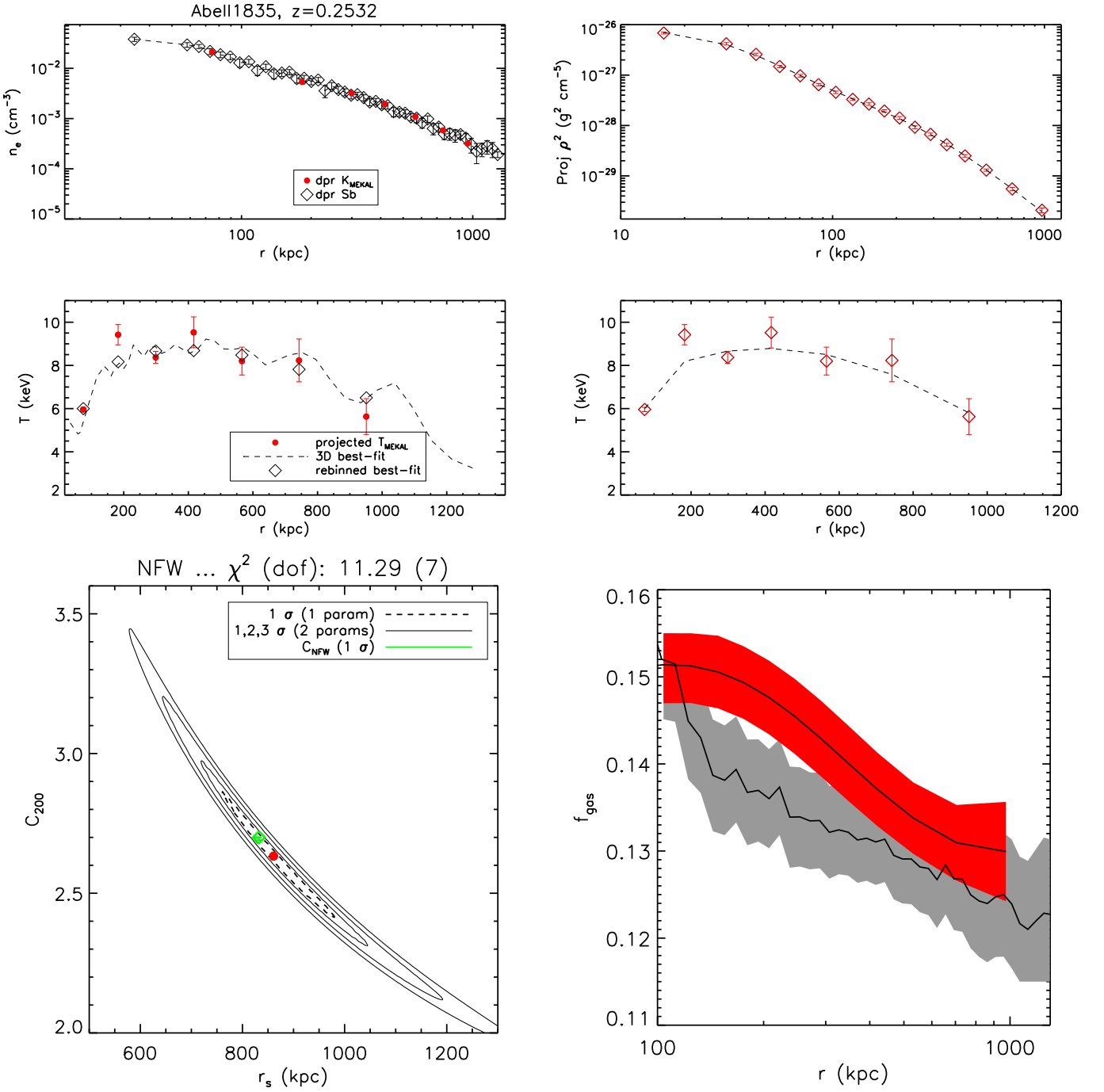


Fig. 2. Example of the results of the two analyses adopted for the mass reconstruction. (*Top and middle panels, left*) Gas density profile as obtained from the deprojection of the surface brightness profile compared to the one recovered from the deprojection of the normalizations of the thermal model in the spectral analysis; observed temperature profile with overplotted the best-fit model (from *Method 1*). (*Top and middle panels, right*) Data (diamonds) and models (dashed lines) of the projected gas density squared and temperature (from *Method 2*). (*Bottom, left*) Constraints in the $r_s - c$ plane with the prediction (in green) obtained by imposing the relation $c_{200} = 4.305/(1+z) \times (M_{200}/10^{14} h_{100}^{-1} M_{\odot})^{-0.098}$ from M08. (*Bottom, right*) Gas mass fraction profile obtained from *Method 1* (gray) and *Method 2* (red).

we perform a simulation within XSPEC: we allow the normalizations of the background components to vary randomly within their errors, we obtain the count rates associated to this fake model and we iterate this procedure. The error on the level of the background components is the width of the distribution of the simulated count rates. Using these values in the outer annulus,

we reconstruct the background profile at all radii. The “photon” components (CXB and galactic foreground) are affected by vignetting in the same way as the source photons and, therefore, dividing by the exposure map effectively corrects also these background components for the vignetting. In order to reconstruct the “photon” background profile, it is thus sufficient to rescale

the count rate for the mean vignetting in the outer annulus (constant blue profile in Fig. 1). On the contrary, the instrumental background does not suffer from vignetting and, therefore, dividing the image by the exposure map “mis-corrects” this component. In order to consider this effect, we divide the corresponding count rate by the vignetting profile (that we derive from the exposure map in the 0.7–1.2 keV), obtaining the growing green curve in Fig. 1. The total background profile (red line in Fig. 1) is the sum of the photon (blue) and instrumental (green) profiles.

The surface brightness profiles $S_b(r)$ have been first extracted from the combined images and binned by requiring a fixed number of 200 counts in each radial bin to preserve all the spatial information available. After the background subtraction, they have been corrected for the PSF smearing. For this purpose, a sum of a cusped β -model and of a β -model (Cavaliere & Fusco-Femiano 1978) with seven free parameters, $f_m(r) = a_0 \times \left[x_1^{-a_2} \times (1 + x_1^2)^{0.5-3a_3+a_2/2} + a_4 (1 + x_2^2)^{0.5-3a_6} \right]$ (with $x_1 = r/a_1$ and $x_2 = r/a_2$), is convolved with the predicted PSF (Ghizzardi 2001) and fitted to the observed profile background-subtracted $S_b(r)$ to obtain the best-fit convolved model $f_c(\bar{a}_i; r)$. Finally, to correct $S_b(r)$ for the PSF-convolution, we apply a correction at each radius \hat{r} where $S_b(r)$ is measured equal to the ratio $f_m(\bar{a}_i; \hat{r})/f_c(\bar{a}_i; \hat{r})$. An example of the results of the procedure is shown in Fig. 1. These corrected profiles are, finally, used in the following analysis up to the radial limit, R_{sp} , beyond which the ratio between the profile and the error on it (including the estimated uncertainty on the measurement of the background) is below 2.

3. Estimates of the mass profiles

We use the profiles of the spectroscopically determined ICM temperature and of the PSF-corrected surface brightness estimated, as described in the previous section, to recover the X-ray gas, the dark and the total mass profiles, under the assumptions of the spherical geometry distribution of the Intracluster Medium (ICM) and that the hydrostatic equilibrium holds between ICM and the underlying gravitational potential. We apply the two following different methods:

- (*Method 1*) This technique is described in Ettori et al. (2002) and has been widely used to recover the mass profiles in recent X-ray studies of both observational (e.g. Morandi et al. 2007; Donnarumma et al. 2009, 2010) and simulated datasets (e.g. Rasia et al. 2006; Meneghetti et al. 2010) against which it has been thoroughly tested.

We summarize here the algorithm adopted and how it uses the observed measurements. Starting from the X-ray surface brightness profile and the radially resolved spectroscopic temperature measurements, this method puts constraints on the parameters of the functional form describing the dark matter M_{DM} , defined as the total mass minus the gas mass (we neglect the marginal contribution from the mass in stars that amounts to about 10-15 % of the gas mass in massive systems –see, e.g., discussion in Ettori et al. 2009 and Andreon 2010–, and is here formally included in the M_{DM} term). In the present work, we adopt a NFW profile:

$$\begin{aligned} M_{\text{DM}}(< r) &= M_{\text{tot}}(< r) - M_{\text{gas}}(< r) = 4\pi r_s^3 \rho_s f(x), \\ \rho_s &= \rho_{c,z} \frac{200}{3} \frac{c^3}{\ln(1+c) - c/(1+c)} \\ f(x) &= \ln(1+x) - \frac{x}{1+x} \end{aligned} \quad (1)$$

where $x = r/r_s$, $\rho_{c,z} = 3H_z^2/8\pi G$ is the critical density at the cluster’s redshift z , $H_z = H_0 \times [\Omega_\Lambda + \Omega_m(1+z)^3]^{1/2}$ is the Hubble constant at redshift z for an assumed flat Universe ($\Omega_m + \Omega_\Lambda = 1$), and the relation $R_{200} = c_{200} \times r_s$ holds.

The two parameters (r_s, c_{200}) are constrained by minimizing a χ^2 statistic defined as

$$\chi_T^2 = \sum_i \frac{(T_{\text{data},i} - T_{\text{model},i})^2}{\epsilon_{T,i}^2} \quad (2)$$

where the sum is done over the annuli of the spectral analysis; T_{data} are the either deprojected or observed temperature measurements obtained in the spectral analysis; T_{model} are either the three-dimensional or projected values of the estimates of T_{gas} recovered from the inversion of the hydrostatic equilibrium equation (see below) for a given gas density and total mass profiles; ϵ_T is the error on the spectral measurements. The gas density profile, n_{gas} , is estimated from the geometrical deprojection (Fabian et al. 1981, Kriss et al. 1983, McLaughlin 1999, Buote 2000, Ettori et al. 2002) of either the measured X-ray surface brightness or the estimated normalization of the thermal model fitted in the spectral analysis (see Fig. 2). In the present study, we consider the observed spectral values of the temperature and evaluate T_{model} by projecting the estimates of T_{gas} over the annuli adopted in the spectral analysis accordingly to the recipe in Mazzotta et al. (2004) and using the gas density profile obtained from the deprojection of the PSF-deconvolved surface brightness profile (see Sect. 2.2). We exclude the deprojected data of the gas density within a cutoff radius of 50 kpc because the influence of the central galaxy is expected to be not negligible, in particular for strong low-entropy core systems. The values of T_{gas} are then obtained from

$$-G\mu m_a \frac{n_{\text{gas}} M_{\text{tot}}(< r)}{r^2} = \frac{d(n_{\text{gas}} \times T_{\text{gas}})}{dr}, \quad (3)$$

where G is the universal gravitational constant, m_a is the atomic mass unit and $\mu=0.61$ is the mean molecular weight in atomic mass unit. To solve this differential equation, we need to define a boundary condition that is here fixed to the value of the pressure measured in the outermost point of the gas density profile, $P_{\text{out}} = P_{\text{gas}}(R_{\text{sp}}) = n_{\text{gas}}(R_{\text{sp}}) \times T_{\text{gas}}(R_{\text{sp}})$, where $T_{\text{gas}}(R_{\text{sp}})$ is estimated by linear extrapolation in the logarithmic space, if required. The systematic uncertainties introduced by this assumption on P_{out} are discussed in the next section. Note that by applying *Method 1* the errors on the gas density do not propagate into the estimates of the parameters of the mass profile and are used both to define the range of the accepted values of P_{out} and to evaluate the uncertainties on the gas mass profiles. The allowed range at 1σ of the two interesting parameters, r_s and c_{200} , is defined from the minimum and the maximum of the values that permit χ_T^2 to be lower or equal to $\min(\chi_T^2) + 1$. The average error on the mass is then the mean of the upper and lower limit obtained at each radius from the allowed ranges at 1σ of r_s and c_{200} . Only for the purpose of estimating the profile of $M_{\text{gas}}(< r)$, and eventually to provide the extrapolated values, the deprojected gas density profile is fitted with the generic functional form described in Ettori et al. (2009) and adapted from the one described in Vikhlinin et al. (2006), $n_{\text{gas}} = n_{\text{gas},0} (r/r_{c,0})^{-\alpha_0} \times (1 + (r/r_{c,0})^2)^{-1.5\alpha_1 + \alpha_0/2} \times (1 + (r/r_{c,1})^{\alpha_2})^{-\alpha_3/\alpha_2}$.

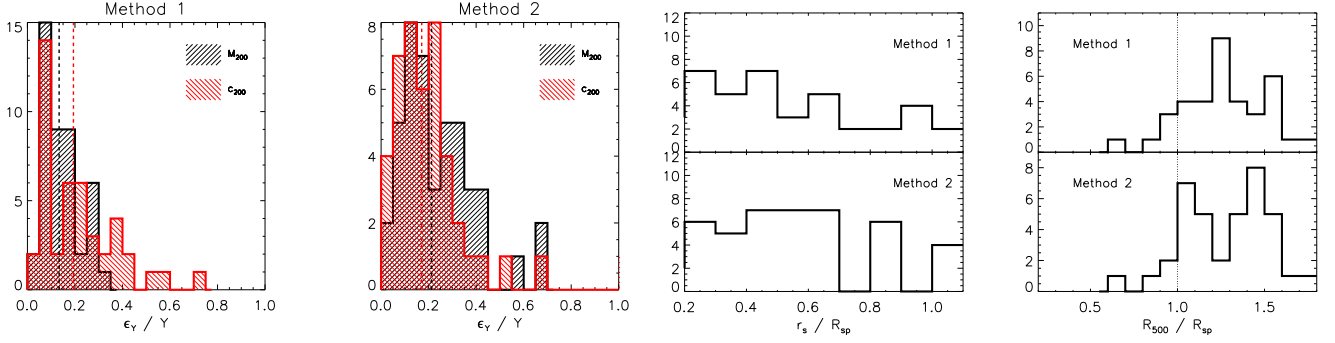


Fig. 3. (First 2 panels on the left) Relative errors on M_{200} (black) and c_{200} (red) estimated by the two methods. The median values are indicated by a dashed line. (3rd and 4th panel from left) Ratios between the best-fit result on the scale radius r_s (3rd panel) and on R_{500} (4th panel) and outermost radius reached with the spatial analysis.

- (*Method 2*) The second method follows the approach described in Humphrey et al. (2006) and Gastaldello et al. (2007) where further details of this technique (in particular in Appendix B of Gastaldello et al. 2007) are provided. We assume parametrizations for the gas density and mass profiles to calculate the gas temperature assuming hydrostatic equilibrium,

$$T(r) = T_0 \frac{n_{\text{gas},0}}{n_{\text{gas}}(r)} - \frac{\mu m_a G}{k_B n_{\text{gas}}(r)} \int_{r_0}^r \frac{n_{\text{gas}} M_{\text{tot}} dr}{r^2}, \quad (4)$$

where n_{gas} is the gas density, $n_{\text{gas},0}$ and T_0 are density and temperature at some “reference” radius r_0 and k_B is Boltzmann’s constant. The n_{gas} and $T(r)$ profiles are fitted simultaneously to the data to constrain the parameters of the gas density and mass models. The parameters of the mass model are obtained from fitting the gas density and temperature data and goodness-of-fit for any mass model can be assessed directly from the residuals of the fit. The quality of the data, in particular of the temperature profile, motivated the use of this approach rather than the default approach of parametrizing the temperature and mass profiles to calculate the gas density used in Gastaldello et al. (2007). We projected the parametrized models of the three-dimensional quantities, n_{gas}^2 and T , and fitted these projected emission-weighted models to the results obtained from our analysis of the data projected on the sky. With respect to the paper cited above, the XSPEC normalization have been derived converting the XMM surface brightness in the 0.7 – 1.2 keV band using the effective area and observed projected temperature and metallicity obtained in the wider radial bins used for spectral extraction. The models have been integrated over each radial bin (rather than only evaluating at a single point within the bin) to provide a consistent comparison. We considered an NFW profile of eq. 1 for fitting the total mass and two models for fitting the gas density profile: the β model (Cavaliere & Fusco-Femiano 1978) a double β model in which a common value of beta is assumed, and a cusped β model (Pratt & Arnaud 2002; Lewis et al. 2003). The last two models have been introduced to account for the sharply peaked surface brightness in the centers of relaxed X-ray systems and they provide the necessary flexibility to parametrize adequately the shape of the gas density profiles of the objects in our sample when the traditional β model fails in fitting the data.

Hereafter, we define $M_{\Delta} = M_{\text{DM}}(< R_{\Delta})$ (i.e. M_{200} is the dark matter enclosed within a sphere where the mean cluster overdensity in dark matter only is 200 times the critical density at the cluster’s redshift) and $f_{\text{gas}}(< R_{\Delta})$ is the ratio between the gas mass, M_{gas} , and the total mass, $M_{\text{tot}} = M_{\text{DM}} + M_{\text{gas}}$, estimated within R_{Δ} , where the overdensity is here estimated by using the *total* (i.e. dark+gas) mass profile.

The best-fit values obtained for an assumed NFW dark matter mass profiles are quoted in Table 2. In Table 3, we present our estimates of R_{200} , R_{500} and the gas mass fraction $f_{\text{gas}} = M_{\text{gas}}/M_{\text{tot}}$, that is hereafter considered within R_{500} to avoid a problematic extrapolation of the data up to R_{200} . In Fig. 3, we show the relative errors provided from the two methods on the estimates of c_{200} and M_{200} . The distribution of the statistical uncertainties is comparable, with median values of 15–20% on both c_{200} and M_{200} with *Method 1* and *Method 2*. Also the distributions of the measurements of c_{200} and M_{200} are very similar, with 1st–3rd quartile range of 2.70 – 5.29 and $4.7 - 11.1 \times 10^{14} M_{\odot}$ with *Method 1* and 3.17 – 5.09 and $4.3 - 9.1 \times 10^{14} M_{\odot}$ with *Method 2*.

Moreover, the two methods show a good agreement between the two estimates of the gas mass fraction $f_{\text{gas}}(< R_{500})$, as shown in Fig. 5. We measure a median (1st, 3rd quartile) of 0.131(0.106, 0.147), and a median relative error of 12%, with *Method 1* and 0.124(0.108, 0.155), and a relative error of 10%, with *Method 2*.

As shown in the last two panels of Fig. 3, we note that the large majority of our data is able to define a scale radius r_s well within the radial range investigated in the spectral and spatial analysis, allowing a quite robust constraints of the fitted parameters.

To rely on the best estimates of the concentration and mass, we define in the following analysis a further subsample by collecting the clusters that satisfy the criterion that the upper value at 1σ of the scale radius, as estimated from the 2 methods, is lower than the upper limit of the spatial extension of the detected X-ray emission, i.e. $(r_s + \epsilon_{r_s}) < R_{\text{sp}}$. Imposing this condition, we select the 26 clusters where a more robust (i.e. with well defined and constrained free parameters) mass reconstruction is achievable.

4. Systematics in the measurements of c_{200} , M_{200} and f_{gas}

The derived quantities c_{200} , M_{200} and $f_{\text{gas}}(< R_{500})$ are measured with a relative statistical error of about 20, 15 and 10 %, respectively.

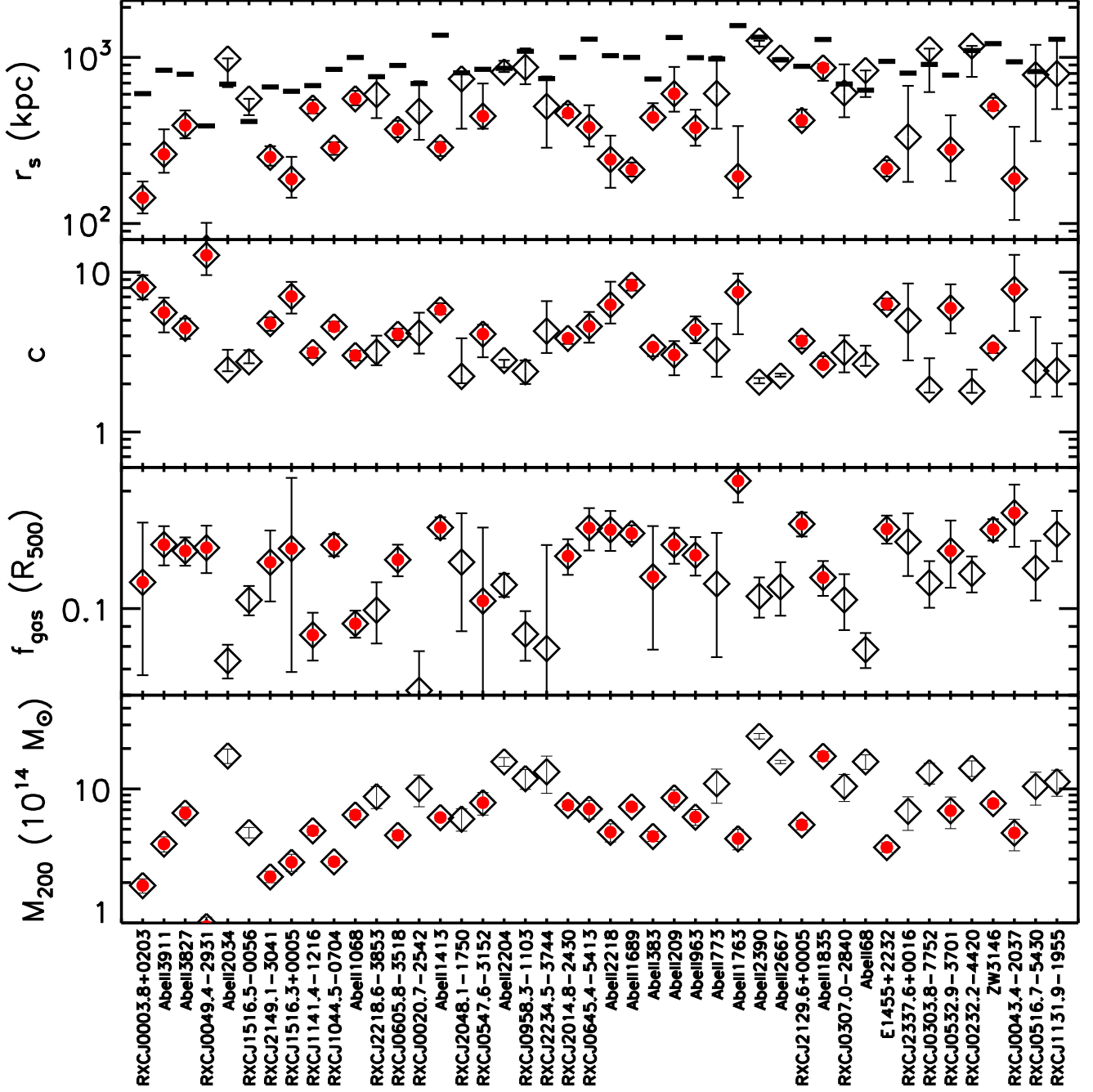


Fig. 4. Best-fit values of r_s , c , gas mass fraction f_{gas} at R_{500} and dark mass M_{DM} within R_{200} as obtained from *Method 1* (diamonds; the ones including red points indicate the objects where the condition $(r_s + \epsilon_{r_s}) < R_{\text{sp}}$ is satisfied by both methods. R_{sp} here plotted as horizontal line in the upper panel).

respectively (see Section 3 and Figures 3 and 5). Here, we investigate the main uncertainties affecting our techniques that will be treated as systematic effects in the following analysis.

We consider two main sources of systematic errors: (i) the analysis of our dataset, both for what concerns the estimates of the gas temperature and the reconstructed gas density profile; (ii) the limitations and assumptions in the techniques adopted for the mass reconstruction.

In Table 4, we summarize our findings tabulated as relative median difference with respect to the estimates obtained with *Method 1*. Overall, we register systematic uncertainties of

$(-5, +1)\%$ on c_{200} , $(-4, +3)\%$ on M_{200} and $(-1, +4)\%$ on $f_{\text{gas}}(< R_{500})$, where these ranges represent the minimum and maximum estimated in the dataset investigated and quoted in Table 4.

4.1. Systematics from the spectral analysis

The ICM properties of the present dataset have been studied through spatially resolved spectroscopic measurements of the gas temperature profile and deprojected, PSF-corrected surface brightness profile as accessible to *XMM-Newton* (see Section 2).

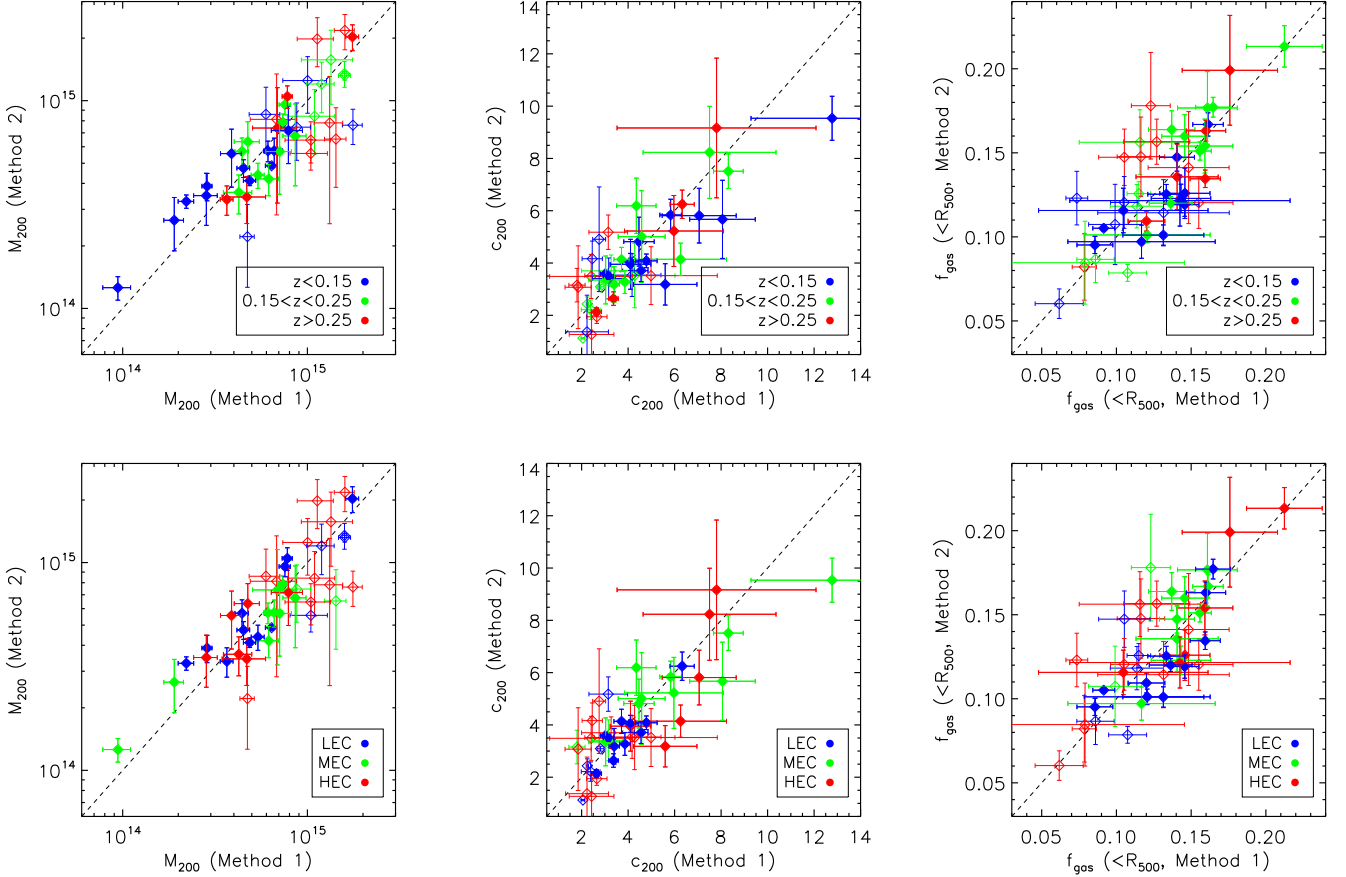


Fig. 5. Estimates of M_{200} (left), c_{200} (center) and $f_{\text{gas}}(< R_{500})$ (right) with the two methods. (Upper panels) The color code indicates the objects at $z < 0.15$ (blue), in the range $0.15 < z < 0.25$ (green) and at $z > 0.25$ (red). (Lower panels) Distribution of Low (LEC), Medium (MEC), High (HEC) Entropy Core systems.

To assess the systematics propagated through the temperature measurements, we present the results obtained with *M2* only, i.e. before any correction introduced from the harder spectra observed with *M1* (see Sect. 2.1). Overall, the systematics are in the order of a few per cent, with the largest offset of about 4 per cent on the concentration and mass measurements at R_{500} and beyond.

When the deprojected spectral values of the gas temperature, instead of the projected ones, are compared with the predictions from the model, we measure differences below 5% (see dataset labelled “ $T_{3\text{D}}$ ”).

On the gas density profile, we investigate the role played from the use of a functional form instead of the values obtained directly from deprojection. To this purpose, we use a revised form of the one introduced from Vikhlinin et al. (2006) to fit the gas density profile and, then, we adopt it as representative of the gas density profile to be put in hydrostatic equilibrium with the gravitational potential in equation 3. The measurements obtained are labelled “fit n_{gas} ” and show discrepancies in the order of 1 per cent or less.

4.2. Systematics from the mass reconstruction methods

With the intention to assess the the bias affecting the reconstructed mass values, we make use of the gas temperature and density profiles through two independent techniques (labelled *Method 1* and *Method 2*), as described in Section 3. With respect

to *Method 1*, *Method 2* provides differences on M_{DM} that are lower than 10 per cent, increasing from about 1 per cent at R_{200} up to 7 per cent at R_{2500} (see Table 4). The bias on f_{gas} remains stable around 3–4 per cent, suggesting that some systematics affect also the estimate of M_{gas} . This is due to the application of two different functional forms in *Method 1* and *Method 2* over a radial range that extends beyond the observational limit (see, e.g., Fig. 3).

The mass reconstruction of *Method 1* depends upon the boundary condition on the gas pressure profile. In particular, to solve the differential equation 3, an outer value on the pressure is fixed to the product of the observed estimate of the gas density profile at the outermost radius and an extrapolated measurement of the gas temperature. Using a grid of values for the pressure obtained from the best-fit results of the gas density and temperature profiles, we evaluate a systematic bias on the mass of about 3 per cent, on the gas mass fraction of 1 per cent, and on c_{200} of about 1 per cent (see dataset labelled “ P_{out} ”).

5. The $c_{200} - M_{200}$ relation

In this section, we investigate the $c_{200} - M_{200}$ relation. We note that our sample has not been selected to be representative of the cluster population in the given redshift range and, in the mean time, does not include only relaxed systems. Therefore, the results here presented on the $c_{200} - M_{200}$ relation have to be just considered for a qualitative comparison with the predictions

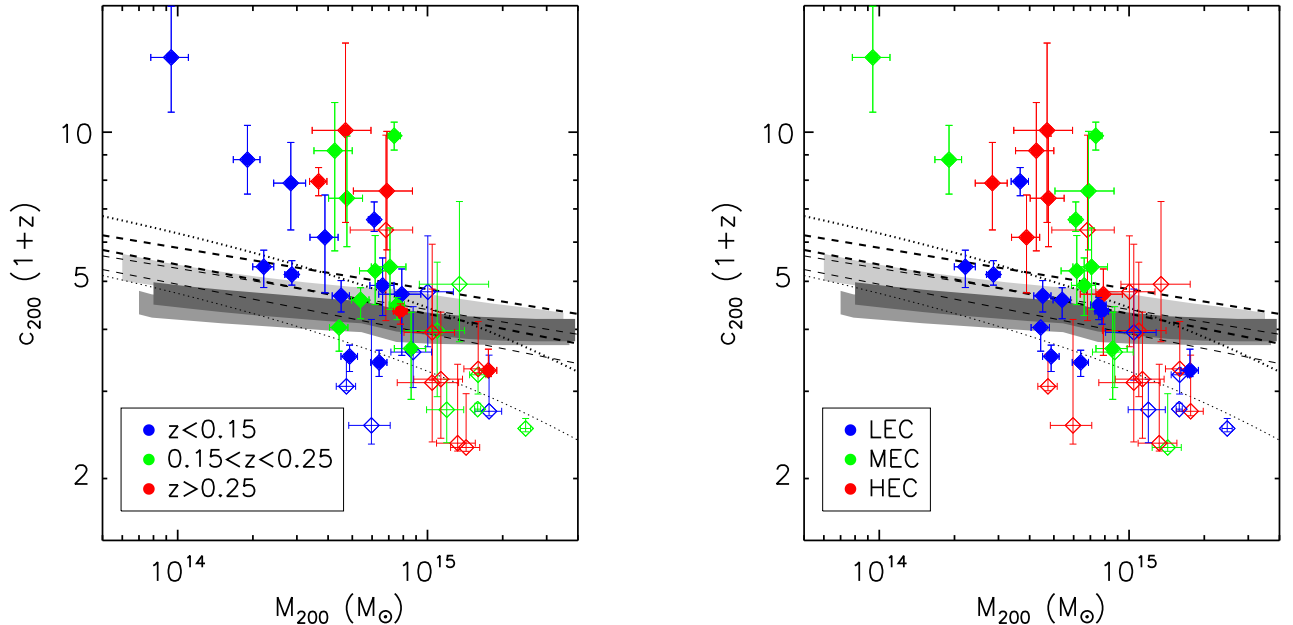


Fig. 6. Data in the plane (c_{200}, M_{200}) used to constrain the cosmological parameters (Ω_m, σ_8) . The dotted lines show the predicted relations from Eke et al. (2001) for a given Λ CDM cosmological model at $z = 0$ (from top to bottom: $\sigma_8 = 0.9$ and $\sigma_8 = 0.7$). The shaded regions show the predictions in the redshift range 0.1 – 0.3 for an assumed cosmological model in agreement with WMAP-1, 5 and 3 years (from the top to the bottom, respectively) from Bullock et al. (2001; after Macciò et al. 2008). The dashed lines indicate the best-fit range at 1σ obtained for relaxed halos in a WMAP-5 years cosmology from Duffy et al. (2008; thin lines: $z = 0.1$, thick lines: $z = 0.3$). Color codes and symbols as in Fig. 5.

from numerical simulations and to assess differences or similarity with previous work on this topic.

As we show in Fig. 6 using the measurements obtained with *Method 1*, the median relation between concentration and total masses for CDM halos as function of redshift is represented well from the analytic algorithms, as in N97, E01 and B01. These models relate the halo properties to the physical mechanism of halo formation. Considering the weak dependence of the halo concentrations on the mass and redshift, Dolag et al. (2004) introduced a two-parameter functional form, $c = c_0 M^B / (1+z)$. We consider this relation in its logarithmic form and fit linearly to our data the expression:

$$\log_{10}(c_{200} \times (1+z)) = A + B \times \log_{10}\left(\frac{M_{200}}{10^{15} M_{\odot}}\right). \quad (5)$$

A minimum in the χ^2 distribution is looked for by taking into account the errors on both the coordinates (we use the routine *FITEXY* in IDL). The errors are assumed to be Gaussian in the logarithmic space, although they are properly measured as Gaussian in the linear space.

We also express our results in term of the concentration c_{15} expected for a dark matter halo of $10^{15} h_{70}^{-1} M_{\odot}$ and equal to 10^4 once the parameters in equation 5 are used. We convert to c_{15} even the results from literature obtained, for instance, at different overdensity, as described in the Appendix.

We measure $A \approx 0.6$ and B systematically lower than -0.1 , with the best-fit results obtained through *Method 1* that prefer, with respect to *Method 2*, a relation with slightly higher normalization (by ~ 10 per cent) and flatter (by 10 – 30 per cent) distribution in mass. In both cases, a total scatter of $\sigma_{\log_{10} c} \approx 0.13$ is measured both in the whole sample of 44 objects, where the sta-

tistical scatter related to the observed uncertainties is still dominant, and in the subsample of 26 selected clusters.

When a slope $B = -0.1$ is assumed, as measured in numerical simulations over one order of magnitude in mass almost independently from the underlying cosmological model (see e.g. Dolag et al. 2004, Macciò et al. 2008), the measured normalizations of the $c_{200} - M_{200}$ relation fall into the range of the estimated values for samples of simulated clusters (see Table 5).

All the values of normalization and slope are confirmed, within the estimated errors, with both the *BCES* bisector method (as described in Akritas & Bershady 1996 and implemented in the routines made available from M.A. Bershady) and a Bayesian method that accounts for measurement errors in linear regression, as implemented in the IDL routine *LINMIX_ERR* by B.C. Kelly (see Kelly 2007). As we quote in Table 5, with these linear regression methods (and after 10^6 bootstrap resampling of the data in *BCES*), we measure a typical error that is larger by a factor 2 – 3 in normalization and up to 6 in the slope than the corresponding values obtained through the covariance matrix of the *FITEXY* method.

These values compare well with the measurements obtained from numerical simulations of DM-only galaxy clusters, although these simulations sample, on average, mass ranges lower than the ones investigated here. Recent work from Shaw et al. (2006) and Macciò et al. (2008) summarize the findings. The slope of the relation, as previously obtained from B01 and D04, lies in the range $(-0.160, -0.083)$, with a preferred value of about -0.1 . The normalizations for low-density Universe with a relatively higher σ_8 , as from WMAP-1, are more in agreement with the observed constraints on, e.g., c_{15} . For instance, M08 find $c_{15} = 4.18, 3.41, 3.56$ for relaxed objects in a background cosmology that matches WMAP-1, 3 and 5 year data,

respectively¹. Shaw et al. (2006) measure $c_{15} = 4.64$ using a flat Universe with $\Omega_m = 0.3$ and $\sigma_8 = 0.95$. D04 for a Λ CDM with $\sigma_8 = 0.9$ require $c_{15} = 4.29$. All these values show the sensitivity of the normalization to the assumed cosmology, that is further discussed in the section where constraints on the cosmological parameters ($\Omega_m - \sigma_8$) will be obtained through the measured $c - M$ relation. Neto et al. (2007) study the statistics of the halo concentrations at $z = 0$ in the *Millennium Simulation* (with an underlying cosmology of $\Omega_m = 1 - \Omega_\Lambda = 0.25, \sigma_8 = 0.9$) and find that a power-law with $B = -0.10$ and $c_{15} = 4.33$ fits fairly well the relation for relaxed objects, with an intrinsic logarithmic scatter for the most massive objects of 0.092 (see their Fig. 7).

We note, however, that, while the normalizations we measure for a fixed slope $B = -0.1$ are well in agreement with the results from numerical simulations, a systematic lower value of the slope is measured, when it is left to vary. To test the robustness of this evidence, we have implemented Monte-Carlo runs using the best-fit central values estimated in N-body simulations (see Appendix B for details). With almost no dependence upon the input values from numerical simulations and using the *FITEXY* technique that provides the results with the most significant deviations from $B \approx -0.1$, we measure in the 3 samples here considered (i.e. all 44 objects, the selected 26 objects, and the only 11 LEC objects) a probability of about 0.5 (1), 20 (42) and 26 (46) per cent, respectively, to obtain a slope lower than the measured $1(3)\sigma$ upper limit. These results confirm that the systematic uncertainties present in the measurements of the concentration and dark mass within R_{200} are still affecting the sample of 44 objects, whereas they are significantly reduced in the selected subsamples.

Our best-fit results are in good agreement also with previous constraints obtained from X-ray measurements in the same cosmology. Pointecouteau et al. (2005) measure $c_{15} \approx 4.5$ and $B = -0.04 \pm 0.03$ in a sample of ten nearby ($z < 0.15$) and relaxed objects observed with *XMM-Newton* in the temperature range 2 – 9 keV. Zhang et al. (2006) measure a steeper slope of -1.5 ± 0.2 , probably affected from few outliers, in the REFLEX-DXL sample of 13 X-ray luminous and distant ($z \sim 0.3$) clusters observed with *XMM-Newton*, that, they claim, are however not well reproduced from a NFW profile. Voigt & Fabian (2006) show a good agreement with B01 results and $B \approx -0.2$ for their estimates of 12 mass profiles of X-ray luminous objects observed with *Chandra* in the redshift range 0.02 – 0.45. A good match with the results in D04, and within the scatter found in simulations, is obtained with 13 low-redshift relaxed systems with T_{gas} in the range 0.7 – 9 keV as measured with *Chandra* in Vikhlinin et al. (2006). Schmidt & Allen (2007), using *Chandra* observations of 34 massive relaxed galaxy clusters, measure $B = -0.45 \pm 0.12$ (95% c.l.), significantly steeper than the value predicted from CDM simulations. Leaving free the redshift dependence that they estimate to be consistent with the $(1+z)^{-1}$ expected evolution, they measure a normalization $c_{15} \approx 5.4 \pm 0.6$ (95% c.l.), definitely higher than our best-fit parameter. Buote et al. (2007) fit the $c - M$ relation from 39 systems in the mass range $0.06 - 20 \times 10^{14} M_\odot$ selected from *Chandra* and *XMM-Newton* archives to be relaxed. Analysing the tabulated values of the 20 galaxy clusters with $M_{200} > 10^{14} M_\odot$, that include the most massive systems from the *XMM-Newton* study of Pointecouteau et al. (2005) and the *Chandra* analysis in Vikhlinin et al. (2006), we measure $B = -0.08 \pm 0.05$ and $c_{15} \approx 5.16 \pm 0.36$.

¹ We refer to Appendix A for a detailed discussion of the conversions adopted

Overall, we conclude however that the slope of the $c - M$ relation cannot be reliably determined from the fitting over a narrow mass range as the one considered in the present work and that, once the slope is fixed to the expected value of $B = -0.1$, the normalization, with estimates of c_{15} in the range 3.8 – 4.6, agrees with results of previous observations and simulations for a calculations in a low density Universe.

5.1. The subsample of Low-Entropy-Core objects

Following Leccardi et al. (2010), we have employed the pseudo-entropy ratio ($\sigma \equiv (T_{\text{IN}}/T_{\text{OUT}}) \times (EM_{\text{IN}}/EM_{\text{OUT}})^{-1/3}$, where IN and OUT define regions within $\approx 0.05 R_{180}$ and encircled in the annulus with bounding radii 0.05-0.20 R_{180} , respectively, and T and EM are the cluster temperature and emission measure) to classify our sample of 44 galaxy clusters accordingly to their core properties. We identify 17 High-Entropy-Core (HEC), 11 Medium-Entropy-Core (MEC) and 16 Low-Entropy-Core (LEC; see Table 1) systems. While the MEC and HEC objects are progressively more disturbed (about 85 per cent of the merging clusters are HEC) and with a core that presents less evidence in the literature of a temperature decrement and a peaked surface brightness profile (intermediate, ICC, and no cool core, NCC, systems), the LEC objects represent the prototype of a relaxed cluster with a well defined cool core (CC in Table 1) at low entropy (see also Cavagnolo et al. 2009). These systems are predicted from numerical simulations to have higher concentrations for given mass, by about 10 per cent, and lower scatter, by about 15-20 per cent, in the $c - M$ relation (e.g. M08, Duffy et al. 2008).

Out of 16, eleven LEC objects are selected under the condition that their scale radius is within the radial coverage of our data. We measure their $c - M$ relation to have slightly lower normalization ($A \approx 0.5 - 0.6, c_{15} \approx 3.2 - 3.7$) and flatter distribution ($B = -0.4 \pm 0.2$) than the one observed in the selected subsample of 26 objects, with a dispersion around the logarithmic value of the concentration of 0.08, that is about 40 per cent lower than the similar value observed in the latter sample. This is consistent in a scenario where disturbed systems have an estimated concentration through the hydrostatic equilibrium equation that is biased higher (and with larger scatter) than in relaxed objects up to a factor of 2 due to the action of the ICM motions (mainly the rotational term in the inner regions and the random gas term above R_{500}), as discussed in Lau et al. (2009; see also Fang et al. 2009, Meneghetti et al. 2010) for galaxy clusters extracted from high-resolution Eulerian cosmological simulations.

6. Cosmological constraints from the measurements of c_{200}, M_{200} , and f_{gas}

N -body simulations have provided theoretical fitting functions that are able to reproduce the distribution of the concentration parameter of the NFW density profile as function of halo mass and redshift (e.g. NFW, E01, B01, N07). Basically, all these semi-empirical prescriptions provide the expected values of the concentration parameter for a given set of cosmological parameters (essentially, the cosmic matter density, Ω_m , and the normalization of the power spectrum on clusters scale, σ_8) for a given mass (the estimated cluster dark mass, M_{200} , in our case) at the measured redshift of the analyzed object. They assume that the concentration reflects the background density of the Universe at the formation time of a given halo. The cosmological model influences the concentration and virial mass because of the cos-

mic background density and the evolution of structure formation. For instance, the NFW model uses two free parameters, (f, C) , to define the collapse redshift at which half of the final mass M is contained in progenitors of mass $\geq fM$, with C representing the ratio between the characteristic overdensity and the mean density of the Universe at the collapse redshift. We use $(f, C) = (0.1, 3000)$.

B01 assume, instead, an alternative model to improve the agreement between the predicted redshift dependence of the concentrations and the results of the numerical simulations by using two free parameters, F and K , where F is still a fixed fraction (0.01 in our study) of a halo mass at given redshift and K indicates the concentration of the halo at the collapse redshift. K has to be calibrated with numerical simulations and is fixed here to be equal to 4 (see also Buote et al. 2007 for a detailed discussion on the role played from the parameters F and K on the prediction of the concentrations as function of the background cosmology and halo masses). M08 have revised this model by assuming that the characteristic density of the halo, that in B01 scales as $(1+z)^3$, is independent of redshift. This correction propagates into the growth factor of the concentration parameter that becomes shallower with respect to the mass dependence at masses higher than $10^{13}h^{-1}M_{\odot}$, permitting larger concentrations at the high-mass end than the original B01 formulation.

The prescription in E01 defines with the only parameter C_{σ} (equal to 28, in our analysis, as suggested in their original work) the collapse redshift z_c through the relation $D(z_c)\sigma_{\text{eff}}(M_s) = C_{\sigma}^{-1}$, where $D(z)$ is the linear growth factor, σ_{eff} is the effective amplitude of the linear power spectrum at $z = 0$ and M_s is the total mass within the radius at which the circular velocity of an NFW halo reaches its maximum and that is equal to 2.17 times the scale radius, r_s .

As tested in high-resolution numerical simulations (see, e.g., N07, M08, Duffy et al. 2008), these 3 formulations provide different predictions over different mass range and redshift: for massive systems a $z < 1$, as the ones under investigation in the present analysis, the original B01 tends to underestimate the concentration at fixed halo mass; its revised version after M08 partially compensate for this difference but still shows some tension with numerically simulated objects (see, e.g., figure 5 in M08); NFW overestimates the concentration, whereas E01 provide good estimates (see, e.g. figure 2 in Duffy et al. 2008) also considering its simpler and more robust formulation, being dependent upon a single parameter that does not need an independent calibration from simulations evolved with a given background cosmology (note, indeed, that as pointed out in M08, both NFW and B01 models have normalizations that, ideally, have to be determined empirically for each assumed cosmology with a dedicated numerical simulation).

Hereafter, we consider E01 as the model of reference and use the other prescriptions as estimate of the systematics affecting our constraints.

In particular, to constrain the cosmological parameters of interest, σ_8 and Ω_m , we calculate first the concentration $c_{200,ijk} = c_{200}(M_i, \Omega_{m,j}, \sigma_{8,k})$ predicted from the model investigated at each cluster redshift for a given grid of values in mass, M_i , cosmic density parameter, $\Omega_{m,j}$, and power spectrum normalization, $\sigma_{8,k}$.

Then, we proceed with the following analysis:

1. a new mass $M_{200,j}$ and concentration $c_{200,j}$ are estimated from the X-ray data for given $\Omega_{m,j}$;

2. we perform a linear interpolation on the theoretical prediction of $c_{200,ijk}$ to associate a concentration $\hat{c}_{200,jk}$ to the new mass $M_{200,j}$ for given $\Omega_{m,j}$ and $\sigma_{8,k}$;
3. we evaluate the merit function χ_c^2

$$\chi_c^2 = \chi_c^2(\Omega_{m,j}, \sigma_{8,k}) = \sum_{\text{data},i} \frac{(c_{200,i} - \hat{c}_{200,jk})^2}{\epsilon_{200,i}^2 + \sigma_c^2}, \quad (6)$$

where $\epsilon_{200,i}$ is the 1σ uncertainty related to the measured $c_{200,i}$ and σ_c is the scatter intrinsic to the mean predicted value $\hat{c}_{200,jk}$ as evaluated in Neto et al. (2007; see their fig. 7 and relative discussion). They estimate in the mass bin $10^{14.25} - 10^{14.75}h^{-1}M_{\odot}$ a logarithmic mean value of the concentration parameter of 0.663, with a dispersion of 0.092, corresponding to a relative uncertainty of 0.139. We take into account these estimates by associating to the expectation of $\hat{c}_{200,jk}$ a scatter equals to $10^{\log \hat{c}_{200,jk} \pm \epsilon_c}$, where $\epsilon_c = 0.139 \times \log \hat{c}_{200,jk}$;

4. a minimum in the χ_c^2 distribution, $\chi_{c,\text{min}}^2$, is evaluated and the regions encompassing $\chi_{c,\text{min}}^2 + (2.3, 6.17, 11.8)$ are estimated to constrain the best-fit values and the $1, 2, 3\sigma$ intervals in the (Ω_m, σ_8) plane shown in Fig. 7. To represent the observed degeneracy in the $\sigma_8 - \Omega_m$ plane, we quote in Table 6 (and show with a dashed line in Fig. 7) the best-fit values of the power-law fit $\sigma_8 \Omega_m^{\gamma} = \Gamma$, obtained by fitting this function on a grid of values estimated, at each assigned Ω_m , the best-fit result, and associated 1σ error, of σ_8 .
5. A further constraint on the Ω_m parameter that allows us to break the degeneracy in the $\sigma_8 - \Omega_m$ plane (as highlighted from the banana-shape of the likelihood contours plotted in Fig. 7) is provided from the gas mass fraction distribution. We use our estimates of $f_{\text{gas}}(< R_{500}) = f_{500}$ from *Method 1* quoted in Table 3. We follow the procedure described in Ettori et al. (2009) and assume: (i) $\Omega_b h_{70}^2 = 0.0462 \pm 0.0012$ and $H_0 = 70.1 \pm 1.3$ from the best-fit results of the joint analysis in Komatsu et al. (2008), (ii) a depletion parameter at R_{500} $b_{500} = 0.874 \pm 0.023$, (iii) a contribution of cold baryons to the total budget $f_{\text{cold}} = 0.18(\pm 0.05)f_{\text{gas}}$. All the quoted errors are at 1σ level. Then, we look for a minimum in the function $\chi_f^2 = \chi_f^2(\Omega_{m,j})$

$$\chi_f^2 = \sum_{\text{data},i} \frac{[f_{500,i}(1 + f_{\text{cold}})/b_{500} - \hat{f}_{\text{bar},j}]^2}{\epsilon_{f,i}^2}, \quad (7)$$

where $\hat{f}_{\text{bar},j} = \Omega_b/\Omega_{m,j}$ and $\epsilon_{f,i}$ is given from the sum in quadrature of all the statistical errors, namely, on $f_{500}, f_{\text{cold}}, H_0, b_{500}$ and Ω_b .

6. We combine the two χ^2 distribution, $\chi_{\text{tot}}^2 = \chi_c^2 + \chi_f^2$, and plot in Fig. 7 the constraints obtained from both χ_c^2 only and χ_{tot}^2 , quoting the best-fit results in Table 6.
7. The effect of the systematic uncertainties, assumed to be normally distributed, is also considered by propagating them in quadrature to the measurements of c_{200} and f_{500} , as obtained from the analysis summarized in Table 4. The constraints obtained after this further correction are indicated with label “+syst” in Table 6.

The cosmological constraints we obtain with 3 different analytic models (E01, B01+M08, NFW) are summarized in Table 6 and likelihood contours for the model of reference E01 are plotted in Fig. 7. To represent the observed degeneracy, we constrain the parameters of the power-law fit $\sigma_8 \Omega_m^{\gamma} = \Gamma$. As expected from the properties of the prescriptions, E01 provides

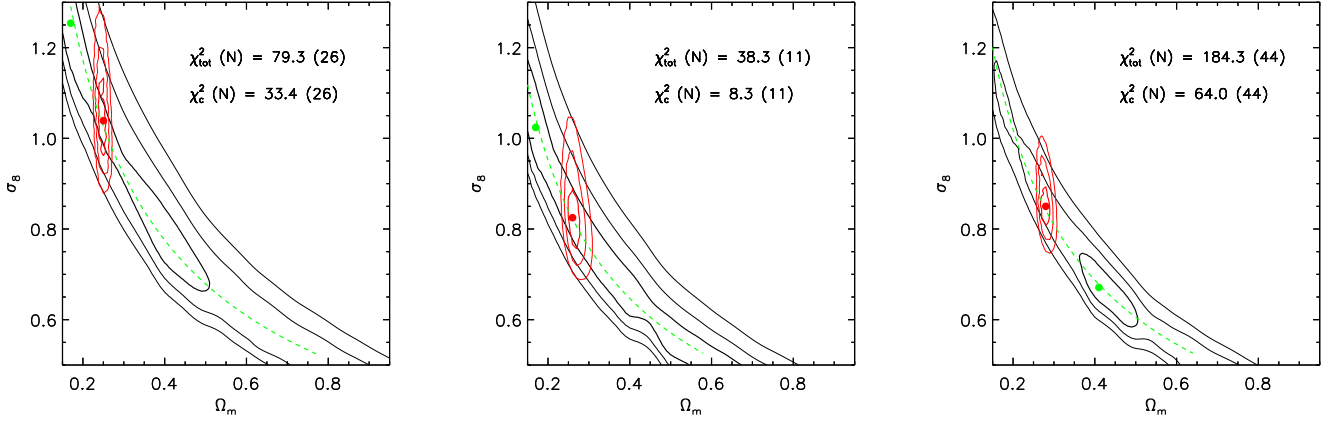


Fig. 7. Cosmological constraints in the (Ω_m, σ_8) plane obtained from equations 6 and 7 by using predictions from the model by Eke et al. (2001). The confidence contours at 1, 2, 3 σ on 2 parameters (solid contours) are displayed. The combined likelihood with the probability distribution provided from the cluster gas mass fraction method is shown in red. The dashed green line indicates the power-law fit $\sigma_8 \Omega_m^\gamma = \Gamma$. The best-fit results are quoted in Table 6. A relative logarithmic scatter of 0.139 (see Sect. 6) is considered in the models. Systematic uncertainties on c_{200} and $f_{\text{gas}}(< R_{500})$ as quoted in Table 4 are also propagated. (*Left*) From the subsample of 26 clusters satisfying the condition $(r_s + \epsilon_{r_s}) < R_{\text{sp}}$; (*center*) from the subsample of the LEC objects; (*right*) from all the 44 clusters.

constraints on σ_8 , for given Ω_m , that lie between the other two, with $\gamma = 0.60 \pm 0.04$ and $\Gamma = 0.44 \pm 0.02$ (at 2 σ level; statistical only). We break the degeneracy of the best-fit values in the (σ_8, Ω_m) plane by assuming that the cluster baryon fraction represents the cosmic value well. We obtain that $\sigma_8 = 1.0 \pm 0.2$ and $\Omega_m = 0.27 \pm 0.01$ (at 2 σ level). When the subsample of 11 LEC clusters, that are expected to be more relaxed and with a well-formed central cooling core, is considered, we measure $\gamma = 0.55 \pm 0.05$, $\Gamma = 0.40 \pm 0.02$, $\sigma_8 = 0.85 \pm 0.16$ and $\Omega_m = 0.27 \pm 0.01$ (at 2 σ level).

We confirm that, assumed correct the ones measured with E01, NFW tends to overestimate the predicted concentrations and, therefore, requires lower normalization σ_8 of the power spectrum, whereas B01+M08 compensate with larger values of σ_8 the underestimate of c_{200} with respect to E01.

We assess the systematics affecting our results by comparing the cosmological constraints obtained by assuming (i) different algorithms to relate the cosmological models to the derived $c - M$ relation, (ii) biases both in the concentration parameter ($b_c = 0.9$), from the evidence in numerical simulations that relaxed halos have a higher concentration by about 10 per cent (e.g. Duffy et al. 2008), and in the dark matter ($b_M = 1.1$) measurements from the evidence provided from hydrodynamical simulations that the hydrostatic equilibrium might underestimate the true mass by 5-20 per cent (e.g. see recent work in Meneghetti et al. 2010). As expected, lower concentrations and higher masses push the best-fit values to lower normalizations of the power spectrum at fixed Ω_m , with an offset of about 10 per cent with $b_c = 0.9$ and of few per cent $b_M = 1.1$ and M_{tot} .

7. Summary and Conclusions

We present the reconstruction of the dark and gas mass from the *XMM-Newton* observations of 44 massive X-ray luminous galaxy clusters in the redshift range 0.1 – 0.3. We estimate a dark ($M_{\text{tot}} - M_{\text{gas}}$) mass within R_{200} in the range (1st and 3rd quartile) $4 - 10 \times 10^{14} M_\odot$, with a concentration c_{200} between 2.7 and 5.3, and a gas mass fraction within R_{500} between 0.11 and 0.16.

By applying the equation of the hydrostatic equilibrium to the spatially resolved estimates of the spectral temperature and normalization, we recover the underlying gravitational potential of the dark matter halo, assumed to be well described from a NFW functional form, with two independent techniques.

Our dataset is able to resolve the temperature profiles up to about $0.6 - 0.8 R_{500}$ and the gas density profile, obtained from the geometrical deprojection of the PSF-deconvolved surface brightness, up to a median radius of $0.9 R_{500}$. Beyond this radial end, our estimates are the results of an extrapolation obtained by imposing a NFW profile for the total mass and different functional forms for M_{gas} .

We estimate, with a relative statistical uncertainty of 15 – 25%, the concentration c_{200} and the mass M_{200} of the dark matter (i.e. total-gas mass) halo. We constrain the $c_{200} - M_{200}$ relation to have a normalization $c_{15} = c_{200} \times (1 + z) \times (M_{200}/10^{15} M_\odot)^{-B}$ of about 2.9 – 4.2 and a slope B between -0.3 and -0.7 (depending on the methods used to recover the cluster parameters and to fit the linear correlation in the logarithmic space), with a relative error of about 5% and 15%, respectively. Once the slope is fixed to the expected value of $B = -0.1$, the normalization, with estimates of c_{15} in the range 3.8 – 4.6, agrees with results of previous observations and simulations for calculations done assuming a low density Universe. We conclude thus that the slope of the $c_{200} - M_{200}$ relation cannot be reliably determined from the fitting over a narrow mass range as the one considered in the present work, although the steeper values measured are not significantly in tension with the results for simulated halos when the subsamples of the most robust estimates are considered (see Sect. 5 and Appendix B). We measure a total scatter in the logarithmic space of about 0.15 at fixed mass. This value decreases to 0.08 when the subsample of LEC clusters is considered, where a slightly lower normalization and flatter distribution is measured. This is consistent in a scenario where disturbed systems have an estimated concentration through the hydrostatic equilibrium equation that is biased higher (and with larger scatter) than in relaxed objects up to a factor of 2 due to the action of the ICM motions (see e.g. Lau et al. 2009).

We put constraints on the cosmological parameters (σ_8, Ω_m) by using the measurements of c_{200} and M_{200} and by comparing the estimated values with the predictions tuned from numerical simulations of CDM universes. In doing that, we propagate the statistical errors (with a relative value of about 15 – 25% at 1σ level) and consider the systematic uncertainties present both in the simulated datasets ($\sim 20\%$) and in our measurements ($\sim 10\%$; see Table 4). To represent the observed degeneracy, we constrain the parameters of the power-law fit $\sigma_8 \Omega_m^\gamma = \Gamma$ and obtain $\gamma = 0.60 \pm 0.03$ and $\Gamma = 0.45 \pm 0.02$ (at 2σ level) when the E01 formalism is adopted. Different formalisms (like the ones in B01, revised after M08, and NFW) induce variations in the best-fit parameters in the order of 20 per cent. A further variation of about 10 per cent occurs if a bias of the order of 10 per cent is considered on the estimates of c_{200} and M_{200} .

We break the degeneracy of the best-fit values in the (σ_8, Ω_m) plane by assuming that the cluster baryon fraction represents the cosmic value well. We obtain that $\sigma_8 = 1.0 \pm 0.2$ and $\Omega_m = 0.26 \pm 0.01$ (at 2σ level; statistical only).

When the subsample of 11 LEC clusters, that are expected to be more relaxed and with a well-formed central cooling core, is considered, we measure $\gamma = 0.56 \pm 0.04$, $\Gamma = 0.39 \pm 0.02$, $\sigma_8 = 0.83 \pm 0.1$ and $\Omega_m = 0.26 \pm 0.02$ (at 2σ level).

All these estimates agree well with similar constraints obtained for an assumed low-density Universe in Buote et al. (2007; $0.76 < \sigma_8 < 1.07$ at 99% confidence for a Λ CDM model with $\Omega_m = 0.3$) and with the results obtained by analysing the mass function of rich galaxy clusters [see, e.g., Wen, Han & Liu (2010) that summarizes recent results obtained by this cosmological tool], showing that the study of the distribution of the measurements in the $c - M_{\text{DM}} - f_{\text{gas}}$ plane provides a valid technique already mature and competitive in the present era of precision cosmology.

However, we highlight the net dependence of our results on the models adopted to relate the properties of a DM halo to the background cosmology. In this context, we urge the N -body community to generate cosmological simulations over a large box to properly predict the expected concentration associated to the massive ($> 10^{14} M_\odot$) DM halos as function of σ_8, Ω_m and redshift. The detailed analysis of the outputs of these datasets will provide the needed calibration to make this technique more reliable and robust.

ACKNOWLEDGEMENTS

The anonymous referee is thanked for suggestions that have improved the presentation of the work. We acknowledge the financial contribution from contracts ASI-INAF I/023/05/0 and I/088/06/0. This research has made use of the X-Rays Clusters Database (BAX) which is operated by the Laboratoire d'Astrophysique de Tarbes-Toulouse (LATT), under contract with the Centre National d'Etudes Spatiales (CNES).

References

Akritas M.G., Bershady M.A., 1996, ApJ, 470, 706
 Allen S.W., Schmidt R.W., Fabian A.C., 2001, MNRAS, 328 L37
 Arnaud K.A., 1996, "Astronomical Data Analysis Software and Systems V", eds. Jacoby G. and Barnes J., ASP Conf. Series vol. 101, 17
 Andreon S., 2010, MNRAS in press (arXiv:1004.2785)
 Arnaud M., Pointecouteau E., Pratt G.W., 2005, A&A, 441, 893
 Baldi A., Ettori S., Mazzotta P., Tozzi P., Borgani S., 2007, ApJ, 666, 835
 Bullock J. S., Kolatt T. S., Sigad Y., Somerville R. S., Kravtsov A. V., Klypin A. A., Primack J. R., Dekel A., 2001, MNRAS, 321, 559
 Buote D.A., 2000, ApJ, 539, 172

Buote D.A., Gastaldello F., Humphrey P.J., Zappacosta L., Bullock J.S., Brighenti F., Mathews W.G., 2007, ApJ, 664, 123
 Cavaliere, A. & Fusco-Femiano, R. 1978, A&A, 70, 677
 Cavagnolo K.W., Donahue M., Voit G.M., Sun M., 2009, ApJS, 182, 12
 Comerford J.M., Natarajan P., 2007, MNRAS, 379, 190
 Croston J.H. et al., 2008, A&A, 487, 431
 Dickey J.M., Lockman F.J., 1990, ARAA, 28, 215
 Dolag K., Bartelmann M., Perrotta F., Baccigalupi C., Moscardini L., Meneghetti M., Tormen G., 2004, A&A, 416, 853
 Donnarumma A., Ettori S., Meneghetti M., Moscardini L., 2009, MNRAS, 398, 438
 Donnarumma A., Ettori S., Meneghetti M. et al., 2010, A&A, in press (arXiv:1002.1625)
 Duffy A.R., Schaye J., Kay S.T., Dalla Vecchia C., 2008, MNRAS, 390, L64
 Eke V. R., Navarro J. F., Steinmetz M., 2001, ApJ, 554, 114
 Ettori S., De Grandi S., Molendi S., 2002, A&A, 391, 841
 Ettori S., Morandi A., Tozzi P., Balestra I., Borgani S., Rosati P., Lovisari L., Terenziani F., 2009, A&A, 501, 61
 Fabian A. C., Hu E. M., Cowie L. L., Grindlay J., 1981, ApJ, 248, 47
 Fang T., Humphrey P., Buote D., 2009, ApJ, 691, 1648
 Finoguenov A., Boehringer H., Zhang Y.-Y., 2005, A&A, 442, 827
 Gao L., Navarro J.F., Cole S., Frenk C.S., White S.D.M., Springel V., Jenkins A.R., Neto A.F., 2008, MNRAS, 387, 536
 Gastaldello F., Buote D. A., Humphrey P. J., Zappacosta L., Bullock, J. S., Brighenti F., Mathews W. G., 2007, ApJ, 669, 158
 Ghizzardi S., 2001, "In Flight Calibration of the PSF for the MOS1 and MOS2 Cameras", EPIC-MOS-TN-11
 Govoni F. et al., 2004, ApJ, 605, 695
 Humphrey P. J., Buote D. A., Gastaldello F., Zappacosta L., Bullock, J. S., Brighenti F., Mathews W. G., 2006, ApJ, 646, 899
 Kelly B.C., 2007, ApJ, 665, 1489
 Kempner J.C., Sarazin C.L., Markevitch M., 2003, ApJ, 593, 291
 Kriss G.A., Cioffi D.F., Canizares C.R., 1983, ApJ, 272, 439
 Kuhlen M., Strigari L. E., Zentner A. R., Bullock J. S., Primack J. R., 2005, MNRAS, 357, 387
 Lau E.T., Kravtsov A.V., Nagai D., 2009, ApJ, 705, 1129
 Leccardi A., Molendi S., 2008, A&A, 486, 359
 Leccardi A., Molendi S., 2008, A&A, 487, 461
 Leccardi A., Rossetti M., Molendi S., 2010, A&A, 510, 82
 Lewis, A. D., Buote, D. A., & Stocke, J. T. 2003, ApJ, 586, 135
 Lin W. P., Jing Y. P., Mao S., Gao L., McCarthy I. G., 2006, ApJ, 651, 636
 Macciò A.V., Dutton A.A., van den Bosch F.C., 2008, MNRAS, 391, 1940
 Mateos S., Saxton R.D., Read A.M., Sembay S., 2009, A&A, 496, 879
 Mazzotta P., Rasia E., Moscardini L., Tormen G., 2004, MNRAS, 354, 10
 Meneghetti M., Rasia E., Merten J., Bellagamba F., Ettori S., Mazzotta P., Dolag K., 2010, A&A, 514, 93
 Morandi A., Ettori S., Moscardini L., 2007, MNRAS, 379, 518
 McLaughlin D.E., 1999, AJ, 117, 2398
 Navarro J.F., Frenk C.S., White S.D.M., 1997, ApJ, 490, 493
 Navarro J.F., Hayashi E., Power C., Jenkins A.R., Frenk C.S., White S.D.M., Springel V., Stadel J., Quinn T.R., 2004, MNRAS, 349, 1039
 Neto A.F., Gao L., Bett P., Cole S., Navarro J.F., Frenk C.S., White S.D.M., Springel V., Jenkins A.R., 2007, MNRAS, 381, 1450
 Pointecouteau E., Arnaud M., Pratt G.W., 2005, A&A, 435, 1
 Pratt, G. W. & Arnaud, M. 2002, A&A, 394, 375
 Pratt G.W. et al., 2007, A&A, 461, 71
 Press W.H., Teukolsky S.A., Vetterling S.A., Flannery B.P., 1992, *Numerical Recipes in Fortran*, Second Edition, p.660
 Rasia E., Ettori S., Moscardini L., Mazzotta P., Borgani S., Dolag K., Tormen G., Cheng L.M., Diaferio A., 2006, MNRAS, 369, 2013
 Sanderson A.J.R., O'Sullivan E., Ponman T.J., 2009, MNRAS, 395, 764
 Schmidt R.W., Allen S.W., 2007, MNRAS, 379, 209
 Shaw L. D., Weller J., Ostriker J. P., Bode P., 2006, ApJ, 646, 815
 Sivanandam S., Zabludoff A.I., Zaritsky D., Gonzalez A.H., Kelson D.D., 2009, ApJ, 691, 1787
 Snowden S.L., Mushotzky R.F., Kuntz K.D., Davis D.S., 2008, A&A, 478, 615
 Vikhlinin A., Kravtsov A., Forman W., Jones C., Markevitch M., Murray S.S., Van Speybroeck L., 2006, ApJ, 640, 691
 Vikhlinin A., Markevitch M., Murray S.S., Jones C., Forman W., Van Speybroeck L., 2005, ApJ, 628, 655
 Voigt L.M., Fabian A.C., 2006, MNRAS, 368, 518
 Voit G.M., 2005, AdSpR, 36, 701
 Wechsler R. H., Bullock J. S., Primack J. R., Kravtsov A. V., Dekel A., 2002, ApJ, 568, 52
 Wen Z.L., Han J.L., Liu F.S., 2010, MNRAS, in press (arXiv:1004.3337)
 Wise M.W., McNamara B.R., Murray S.S., 2004, ApJ, 601, 184
 Wojtak R., Łokas E.L., 2010, MNRAS, submitted (arXiv:1004.3771)

Zhang Y.-Y., Böhringer H., Finoguenov A., Ikebe Y., Matsushita K., Schuecker P., Guzzo L., Collins C. A., 2006, A&A, 456, 35
 Zhang Y.-Y. et al., 2010, ApJ, 711, 1033

Appendix A: Conversion between different overdensity and $c - M$ relations

The total mass within a given overdensity Δ is defined in the present work as

$$M_{\Delta} = \frac{4}{3}\pi R_{\Delta}^3 \Delta \rho_{c,z}, \quad (\text{A.1})$$

where $\rho_{c,z} = 3H_z^2/(8\pi G)$ is the critical density of the Universe at the cluster's redshift z , $R_{\Delta} = c_{\Delta} r_s$ is the radius within which the mean cluster overdensity is Δ times $\rho_{c,z}$ and the relation with the concentration c_{Δ} and the scale radius r_s holds by definition of the NFW mass profile. We assume $\Delta = 200$. Hereafter, we refer to Δ as any other assumed overdensity. In case it is referred to the background density of the Universe, $\rho_b = \Omega_{m,z}\rho_{c,z}$, it is straightforward to correct Δ by $\Omega_{m,z} = \Omega_m(1+z)^3/H_z^2$ to recover the definition in equation A.1.

To convert the tabulated values to our definition of the $c - M$ relation,

$$c_{200} = \frac{c_{15}}{1+z} \left(\frac{M_{200}}{M_{15}} \right)^B, \quad (\text{A.2})$$

where $M_{15} = 10^{15} h_{70}^{-1} M_{\odot}$, we proceed as follows:

1. by definition, $M_{\Delta}/(R_{\Delta}^3 \Delta)$ is constant and R_{Δ}/c_{Δ} is fixed from the measurement of the scale radius. Therefore, we can write

$$\frac{M_{\Delta}}{c_{\Delta}^3} = \frac{M_{200}}{c_{200}^3} \frac{\Delta}{200} \quad (\text{A.3})$$

2. c_{Δ} and c_{200} are related through the assumed NFW mass density profile

$$\left(\frac{c_{200}}{c_{\Delta}} \right)^3 \frac{\ln(1+c_{\Delta}) - c_{\Delta}/(1+c_{\Delta})}{\ln(1+c_{200}) - c_{200}/(1+c_{200})} = \frac{\Delta}{200}. \quad (\text{A.4})$$

This function is monotonic and easily to resolve numerically to estimate $C = c_{\Delta}/c_{200}$, that is a quantity that depends mostly on Δ and only marginally on the guessed c_{200} , as shown in Fig. A.1. For instance, for $\Delta = 178\Omega_{m,z}^{0.45}$, which estimate the virial overdensity predicted from the spherical collapse model in a flat Universe with a contribution from dark energy (Eke et al. 2001), $C = 1.34$ and 1.22 at $z = 0$ and $z = 0.3$, respectively, for $\Omega_m = 0.3$, with deviations within 2% in the range $c_{200} = 3 - 6$.

3. for a given relation $c_{\Delta} = c_0(1+z)^{-1} (M_{\Delta}/M_*)^B$, we substitute the above relations to obtain after simple algebraical operations:

$$c_{200} = \frac{c_0 C^{3B-1}}{1+z} \left(\frac{\Delta}{200} \frac{M_{15}}{M_*} \frac{M_{200}}{M_{15}} \right)^B, \quad (\text{A.5})$$

or

$$c_{15} = c_0 C^{3B-1} \left(\frac{\Delta}{200} \frac{M_{15}}{M_*} \right)^B. \quad (\text{A.6})$$

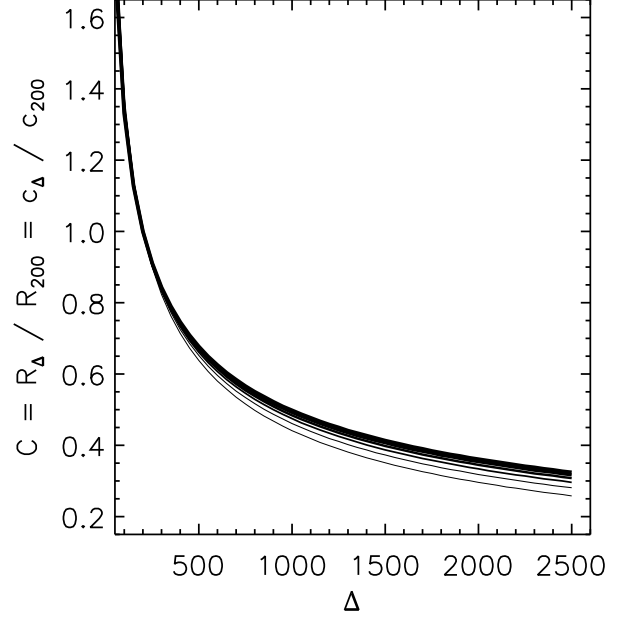


Fig. A.1. Numerical solution to equation A.4 for an assumed c_{200} in the range 3 – 8 (from the thinnest to the thickest line).

Appendix B: Monte-Carlo realizations of the $c_{200} - M_{200}$ relation

We have run Monte-Carlo (MC) simulations to test the robustness of the observed deviations in the $c_{200} - M_{200}$ relation described in Section 5. We have used as input values the best-fit results (defined in the following analysis as \bar{c}_{15} and B) obtained in the numerical simulations from Neto et al. (2007; see their equations 4 and 5) and Macciò et al. (2008; see Table A1 and A2) and listed in Tab. 5. We have considered the results for both the complete sample and the relaxed objects only. To each cluster in our sample with measured mass $M_{200,i}$ and redshift z_i , we assign the concentration $c_{200,i}$ defined as

$$c_{200,i} = 10^{l_i} \quad (\text{B.1})$$

$$l_i = \log_{10} \left[\bar{c}_{15} \times (M_{200,i}/10^{15})^B / (1+z_i) \right] + R \times \epsilon_{\log c},$$

where R is a random value extracted from a Gaussian distribution and $\epsilon_{\log c}$ is the scatter in the log-Normal distribution measured in the numerical simulations (~ 0.13 for samples including all the simulated objects and ~ 0.1 for the sample of the relaxed ones; the actual values are quoted in N07 and in Table A1 and A2 of M08). We assume that (1) our LEC objects follow the distribution obtained for relaxed simulated clusters; (2) all the remaining clusters follow the distribution estimated for the complete simulated halo sample; (3) the 3 samples considered in our analysis with 44, 26 and 11 clusters, respectively, are built considering whether each object is a LEC and/or has an upper limit at 1σ on the scale radius lower than R_{sp} , as discussed in Section 5. To be conservative in our approach, we fit equation 5 to the distribution in the $c_{200} - M_{200}$ with the FITEXY technique that is the one that provides the most significant deviations from the results obtained in numerical simulations. We repeat this process 10,000 times and obtain the plots shown in Fig. B.1 for each of the case investigated. In Table B.1, we summarize our finding from which we conclude that, while the best-fit values estimated

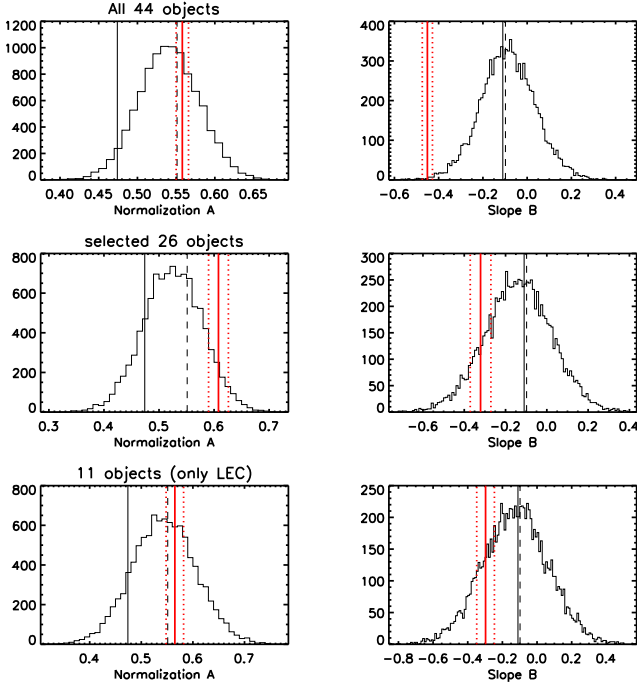


Fig. B.1. Distribution of the best-fit values of the normalization A and slope B after 10,000 MC realizations. The input values (in these plots from M08 / WMAP-5) are indicated with vertical solid (for all the simulated objects) and dashed (for the relaxed ones) lines. The red solid line represents the central value for the corresponding sample as quoted in Table 5. The red dotted lines show the 1σ uncertainties.

for the samples of 26 and 11 clusters are within the overall distribution expected in numerical simulations, the sample of 44 clusters provides results on the slope B that lie on the lower end of the distribution, as probable consequence of the uncertainties present both on the estimates of c_{200} and M_{200} for the 18 clusters that are indeed not selected for the further analysis and on the residual bias affecting the measurements of c_{200} under the hypothesis of the hydrostatic equilibrium (see Section 5.1 and, e.g., Lau et al. 2009).

Table 2. Results on the mass reconstruction.

Cluster	R_{sp} kpc	R_{xsp} kpc	r_s kpc	<i>Method 1</i>			<i>Method 2</i>				
				c_{200}	M_{200} $10^{14} M_{\odot}$	χ^2_T (N)	r_s kpc	c_{200}	M_{200} $10^{14} M_{\odot}$	χ^2_T (N)	χ^2_n (N)
RXCJ0003.8+0203	605	414	143^{+36}_{-28}	$8.06^{+1.52}_{-1.30}$	1.90 ± 0.23	2.3(7)	227 ± 77	5.67 ± 1.49	2.66 ± 0.76	2.7(6)	7.1(11)
Abell3911	836	754	261^{+108}_{-59}	$5.59^{+1.35}_{-1.39}$	3.88 ± 0.50	10.2(9)	517 ± 211	3.18 ± 0.79	5.56 ± 1.73	10.8(8)	9.1(13)
Abell3827	792	767	390^{+89}_{-64}	$4.47^{+0.67}_{-0.64}$	6.61 ± 0.73	3.4(9)	345 ± 66	4.82 ± 0.94	5.74 ± 0.86	2.5(8)	19.8(25)
RXCJ0049.4-2931	386	371	71^{+30}_{-19}	$12.77^{+3.80}_{-3.18}$	0.94 ± 0.16	5.7(6)	104 ± 17	9.54 ± 0.84	1.26 ± 0.16	6.2(5)	7.6(6)
Abell2034	690	866	979^{+7}_{-317}	$2.46^{+0.81}_{-0.66}$	17.64 ± 2.17	7.7(9)	436 ± 110	4.16 ± 0.68	7.62 ± 1.47	9.4(8)	62.1(22)
RXCJ1516.5-0056	411	502	563^{+0}_{-114}	$2.75^{+0.49}_{-0.66}$	4.73 ± 0.42	8.1(7)	245 ± 139	4.91 ± 2.00	2.22 ± 0.95	4.4(6)	5.6(4)
RXCJ2149.1-3041	663	513	251^{+41}_{-28}	$4.79^{+0.43}_{-0.49}$	2.21 ± 0.21	24.6(7)	335 ± 22	4.08 ± 0.26	3.28 ± 0.24	8.0(6)	17.2(11)
RXCJ1516.3+0005	624	514	185^{+67}_{-42}	$7.06^{+1.64}_{-1.54}$	2.84 ± 0.41	2.8(7)	240 ± 92	5.81 ± 1.05	3.49 ± 0.98	2.7(6)	15.5(7)
RXCJ1141.4-1216	676	519	496^{+60}_{-36}	$3.15^{+0.19}_{-0.24}$	4.88 ± 0.37	13.0(7)	422 ± 19	3.50 ± 0.13	4.12 ± 0.22	3.3(6)	6.6(6)
RXCJ1044.5-0704	847	566	286^{+23}_{-27}	$4.56^{+0.34}_{-0.25}$	2.86 ± 0.18	13.3(7)	388 ± 63	3.71 ± 0.42	3.88 ± 0.58	8.0(6)	14.8(9)
Abell1068	998	1026	564^{+66}_{-49}	$3.02^{+0.20}_{-0.22}$	6.40 ± 0.48	8.0(9)	432 ± 8	3.59 ± 0.05	4.86 ± 0.13	5.0(8)	17.4(18)
RXCJ2218.6-3853	764	587	597^{+184}_{-166}	$3.16^{+0.85}_{-0.53}$	8.76 ± 1.62	9.9(7)	524 ± 175	3.41 ± 0.78	7.46 ± 2.29	7.6(6)	1.1(7)
RXCJ0605.8-3518	893	598	369^{+47}_{-39}	$4.10^{+0.54}_{-0.34}$	4.51 ± 0.36	17.8(7)	380 ± 43	4.04 ± 0.32	4.73 ± 0.46	9.4(6)	16.6(8)
RXCJ0020.7-2542	695	603	473^{+245}_{-154}	$4.17^{+1.41}_{-1.07}$	10.03 ± 2.67	17.7(7)	599 ± 205	3.54 ± 0.82	12.50 ± 3.79	5.2(6)	18.2(10)
Abell1413	1360	793	287^{+23}_{-32}	$5.83^{+0.57}_{-0.35}$	6.12 ± 0.32	6.3(8)	280 ± 40	5.84 ± 0.60	5.73 ± 0.65	5.3(7)	6.7(14)
RXCJ2048.1-1750	806	619	742^{+80}_{-370}	$2.23^{+1.63}_{-0.21}$	5.96 ± 1.12	2.7(7)	1365 ± 578	1.37 ± 1.40	8.59 ± 3.01	3.0(6)	22.6(12)
RXCJ0547.6-3152	847	624	443^{+253}_{-71}	$4.10^{+0.59}_{-0.17}$	7.89 ± 1.51	4.7(7)	445 ± 158	3.95 ± 0.95	7.18 ± 2.20	2.9(6)	10.9(16)
Abell2204	858	837	816^{+137}_{-0}	$2.81^{+0.02}_{-0.28}$	15.93 ± 1.19	58.3(8)	696 ± 30	3.09 ± 0.09	13.19 ± 0.64	33.7(7)	4.4(19)
RXCJ0958.3-1103	1088	639	872^{+260}_{-183}	$2.39^{+0.42}_{-0.39}$	11.94 ± 2.02	3.8(7)	942 ± 223	2.21 ± 0.37	12.03 ± 3.28	1.9(6)	6.4(7)
RXCJ2234.5-3744	745	640	506^{+261}_{-220}	$4.28^{+2.31}_{-1.16}$	13.42 ± 4.15	1.4(7)	648 ± 271	3.52 ± 1.23	15.72 ± 6.11	1.7(6)	6.7(13)
RXCJ2014.8-2430	999	878	462^{+59}_{-25}	$3.86^{+0.15}_{-0.30}$	7.56 ± 0.53	28.6(8)	589 ± 70	3.28 ± 0.44	9.57 ± 1.02	13.1(7)	12.0(10)
RXCJ0645.4-5413	1287	904	380^{+135}_{-89}	$4.58^{+1.06}_{-0.96}$	7.08 ± 1.12	7.7(8)	323 ± 174	5.01 ± 1.76	5.69 ± 2.14	12.4(7)	4.3(13)
Abell2218	1024	716	243^{+95}_{-79}	$6.26^{+2.46}_{-1.48}$	4.76 ± 0.74	11.3(7)	404 ± 129	4.14 ± 0.62	6.35 ± 1.57	10.0(6)	6.3(10)
Abell1689	999	974	211^{+22}_{-19}	$8.31^{+0.64}_{-0.63}$	7.36 ± 0.44	16.3(8)	238 ± 28	7.51 ± 0.66	7.88 ± 0.75	9.2(7)	25.3(21)
Abell383	740	589	435^{+95}_{-0}	$3.40^{+0.03}_{-0.42}$	4.43 ± 0.37	27.0(6)	505 ± 81	3.18 ± 0.68	5.71 ± 0.91	11.5(5)	4.1(4)
Abell209	1317	1069	604^{+272}_{-133}	$3.03^{+0.67}_{-0.77}$	8.60 ± 1.23	8.8(8)	504 ± 311	3.35 ± 0.92	6.77 ± 2.87	8.5(7)	12.3(16)
Abell963	995	813	377^{+107}_{-83}	$4.35^{+0.94}_{-0.76}$	6.17 ± 0.83	5.7(7)	233 ± 58	6.19 ± 1.06	4.20 ± 0.72	4.6(6)	7.7(11)
Abell773	977	846	605^{+408}_{-233}	$3.27^{+1.45}_{-1.05}$	10.94 ± 3.12	6.6(7)	489 ± 188	3.70 ± 0.61	8.42 ± 2.88	5.1(6)	12.0(9)
Abell1763	1553	1136	192^{+194}_{-49}	$7.50^{+2.30}_{-3.41}$	4.25 ± 0.74	8.1(8)	165 ± 91	8.23 ± 1.76	3.62 ± 0.77	3.2(7)	9.2(12)
Abell2390	1322	1156	1258^{+0}_{-95}	$2.06^{+0.12}_{-0.04}$	24.71 ± 1.16	11.6(8)	2973 ± 13	1.13 ± 0.03	53.68 ± 3.48	5.3(7)	15.6(12)
Abell2667	966	885	993^{+0}_{-48}	$2.24^{+0.08}_{-0.02}$	15.88 ± 0.45	4.8(7)	867 ± 116	2.43 ± 0.27	13.51 ± 1.92	2.1(6)	1.7(6)
RXCJ2129.6+0005	883	702	418^{+68}_{-37}	$3.71^{+0.27}_{-0.38}$	5.40 ± 0.44	3.4(6)	350 ± 55	4.14 ± 0.46	4.39 ± 0.61	2.0(5)	5.1(7)
Abell1835	1281	950	866^{+46}_{-143}	$2.64^{+0.34}_{-0.89}$	17.53 ± 1.41	10.9(7)	1122 ± 157	2.14 ± 0.16	20.29 ± 2.89	9.8(6)	6.2(12)
RXCJ0307.0-2840	691	951	611^{+297}_{-175}	$3.15^{+0.88}_{-0.78}$	10.44 ± 2.39	5.0(7)	301 ± 69	5.18 ± 0.66	5.57 ± 0.94	5.2(6)	2.5(5)
Abell68	634	746	834^{+0}_{-257}	$2.65^{+0.82}_{-0.66}$	15.96 ± 1.97	4.4(6)	1262 ± 234	1.94 ± 0.25	21.78 ± 4.20	5.0(5)	12.6(7)
E1455+2232	946	752	214^{+26}_{-22}	$6.32^{+0.53}_{-0.51}$	3.66 ± 0.29	2.7(6)	210 ± 35	6.25 ± 0.54	3.35 ± 0.54	1.3(5)	3.9(7)
RXCJ2337.6+0016	803	1004	332^{+342}_{-154}	$4.99^{+3.52}_{-2.18}$	6.81 ± 1.91	1.1(7)	499 ± 490	3.52 ± 1.11	8.13 ± 5.31	2.3(6)	1.5(4)
RXCJ0303.8-7752	906	1007	1115^{+14}_{-497}	$1.85^{+1.04}_{-0.09}$	13.21 ± 2.33	5.7(7)	563 ± 525	3.07 ± 1.58	7.82 ± 5.26	4.9(6)	2.5(5)
RXCJ0532.9-3701	781	787	278^{+170}_{-98}	$5.97^{+2.43}_{-1.82}$	6.88 ± 1.83	3.3(6)	325 ± 195	5.22 ± 1.36	7.39 ± 4.17	3.1(5)	10.2(6)
RXCJ0232.2-4420	1099	1032	1172^{+0}_{-409}	$1.80^{+0.66}_{-0.04}$	14.28 ± 1.90	12.4(7)	515 ± 257	3.15 ± 0.64	6.53 ± 2.71	13.0(6)	3.0(6)
ZW3146	1210	820	510^{+61}_{-31}	$3.37^{+0.15}_{-0.26}$	7.79 ± 0.49	27.5(6)	719 ± 86	2.64 ± 0.26	10.48 ± 1.30	18.1(5)	4.3(15)
RXCJ0043.4-2037	940	823	186^{+196}_{-81}	$7.80^{+5.05}_{-3.51}$	4.70 ± 1.24	10.7(6)	142 ± 85	9.16 ± 2.67	3.44 ± 0.88	7.7(5)	2.4(7)
RXCJ0516.7-5430	821	1061	785^{+405}_{-472}	$2.41^{+2.82}_{-0.78}$	10.44 ± 2.88	1.8(7)	462 ± 261	3.49 ± 0.84	6.46 ± 1.45	2.1(6)	2.3(7)
RXCJ1131.9-1955	1285	1091	797^{+497}_{-309}	$2.43^{+1.36}_{-0.76}$	11.31 ± 2.50	6.9(7)	1839 ± 629	1.27 ± 0.84	19.82 ± 5.26	3.0(6)	4.1(5)

Notes. We quote the name of the object, the upper limit of the radial range investigated in the spatial (R_{sp}) and spectral analysis (R_{xsp}), the best-fit values of the scale radius, the concentration parameters, M_{200} and minimum χ^2 with the corresponding degrees of freedom. In the case of *Method 2*, we quote two minimum χ^2 , corresponding to the minima obtained from the simultaneous fits of the temperature (χ^2_T) and gas density (χ^2_n) profiles.

Table 3. Estimates of R_{200} , R_{500} and the gas mass fraction.

Cluster	<i>Method 1</i>			<i>Method 2</i>		
	R_{200} kpc	R_{500} kpc	f_{gas} < R_{500}	R_{200} kpc	R_{500} kpc	f_{gas} < R_{500}
RXCJ0003.8+0203	1231 ± 65	824 ± 38	0.117 ± 0.049	1360 ± 122	899 ± 50	0.097 ± 0.010
Abell3911	1589 ± 88	1044 ± 41	0.146 ± 0.017	1773 ± 155	1130 ± 75	0.126 ± 0.015
Abell3827	1894 ± 84	1228 ± 45	0.140 ± 0.012	1823 ± 87	1184 ± 40	0.147 ± 0.008
RXCJ0049.4-2931	980 ± 59	666 ± 37	0.143 ± 0.020	1071 ± 39	721 ± 29	0.123 ± 0.008
Abell2034	2491 ± 140	1569 ± 75	0.073 ± 0.007	1957 ± 108	1267 ± 114	0.123 ± 0.016
RXCJ1516.5-0056	1668 ± 65	1039 ± 38	0.105 ± 0.009	1309 ± 159	845 ± 98	0.120 ± 0.015
RXCJ2149.1-3041	1298 ± 52	846 ± 30	0.131 ± 0.027	1452 ± 36	942 ± 26	0.101 ± 0.006
RXCJ1516.3+0005	1416 ± 95	940 ± 54	0.142 ± 0.074	1502 ± 107	991 ± 81	0.122 ± 0.015
RXCJ1141.4-1216	1635 ± 55	1047 ± 31	0.086 ± 0.012	1551 ± 27	1003 ± 23	0.095 ± 0.005
RXCJ1044.5-0704	1399 ± 35	923 ± 19	0.146 ± 0.009	1531 ± 72	996 ± 21	0.119 ± 0.007
Abell1068	1772 ± 57	1140 ± 31	0.091 ± 0.007	1645 ± 13	1061 ± 7	0.105 ± 0.002
RXCJ2218.6-3853	1991 ± 159	1275 ± 84	0.099 ± 0.018	1900 ± 167	1222 ± 132	0.107 ± 0.024
RXCJ0605.8-3518	1613 ± 64	1057 ± 29	0.133 ± 0.012	1643 ± 49	1071 ± 25	0.125 ± 0.006
RXCJ0020.7-2542	2023 ± 228	1329 ± 124	0.062 ± 0.016	2182 ± 200	1415 ± 82	0.060 ± 0.009
Abell1413	1837 ± 64	1207 ± 21	0.161 ± 0.010	1809 ± 58	1188 ± 28	0.167 ± 0.007
RXCJ2048.1-1750	1792 ± 155	1110 ± 80	0.132 ± 0.044	2008 ± 269	1187 ± 109	0.114 ± 0.020
RXCJ0547.6-3152	1921 ± 161	1251 ± 85	0.105 ± 0.057	1882 ± 168	1219 ± 81	0.116 ± 0.013
Abell2204	2450 ± 79	1549 ± 44	0.115 ± 0.008	2319 ± 33	1477 ± 47	0.126 ± 0.007
RXCJ0958.3-1103	2183 ± 174	1366 ± 87	0.086 ± 0.013	2191 ± 174	1363 ± 106	0.087 ± 0.014
RXCJ2234.5-3744	2237 ± 293	1474 ± 164	0.079 ± 0.067	2377 ± 294	1542 ± 159	0.085 ± 0.025
RXCJ2014.8-2430	1935 ± 56	1245 ± 32	0.136 ± 0.014	2067 ± 70	1323 ± 16	0.120 ± 0.004
RXCJ0645.4-5413	1919 ± 133	1243 ± 65	0.161 ± 0.020	1811 ± 183	1174 ± 83	0.177 ± 0.022
Abell2218	1671 ± 120	1100 ± 53	0.159 ± 0.019	1820 ± 120	1122 ± 66	0.154 ± 0.016
Abell1689	1892 ± 40	1279 ± 24	0.156 ± 0.008	1946 ± 54	1304 ± 21	0.151 ± 0.005
Abell383	1577 ± 79	1015 ± 39	0.121 ± 0.042	1697 ± 100	1090 ± 17	0.101 ± 0.005
Abell209	2006 ± 125	1267 ± 57	0.146 ± 0.015	1873 ± 197	1196 ± 54	0.160 ± 0.013
Abell963	1750 ± 95	1153 ± 50	0.137 ± 0.015	1586 ± 74	1049 ± 36	0.164 ± 0.011
Abell773	2100 ± 257	1350 ± 130	0.116 ± 0.041	1959 ± 170	1140 ± 92	0.156 ± 0.019
Abell1763	1644 ± 105	1079 ± 52	0.212 ± 0.025	1575 ± 88	1028 ± 39	0.213 ± 0.012
Abell2390	2735 ± 63	1695 ± 36	0.108 ± 0.013	3484 ± 67	2026 ± 57	0.079 ± 0.005
Abell2667	2374 ± 36	1478 ± 22	0.114 ± 0.018	2259 ± 103	1417 ± 72	0.118 ± 0.013
RXCJ2129.6+0005	1711 ± 60	1099 ± 30	0.165 ± 0.012	1619 ± 63	1042 ± 16	0.177 ± 0.006
Abell1835	2433 ± 86	1540 ± 46	0.120 ± 0.012	2539 ± 100	1583 ± 34	0.109 ± 0.006
RXCJ0307.0-2840	2030 ± 199	1302 ± 103	0.105 ± 0.017	1695 ± 78	1114 ± 59	0.147 ± 0.017
Abell68	2293 ± 127	1457 ± 71	0.079 ± 0.008	2549 ± 165	1489 ± 155	0.082 ± 0.020
E1455+2232	1484 ± 46	980 ± 26	0.160 ± 0.013	1445 ± 59	954 ± 14	0.163 ± 0.006
RXCJ2337.6+0016	1779 ± 192	1178 ± 96	0.148 ± 0.027	1894 ± 278	1225 ± 173	0.141 ± 0.033
RXCJ0303.8-7752	2191 ± 179	1347 ± 93	0.116 ± 0.016	1888 ± 301	1203 ± 122	0.148 ± 0.024
RXCJ0532.9-3701	1784 ± 179	1186 ± 102	0.141 ± 0.027	1835 ± 233	1207 ± 105	0.136 ± 0.019
RXCJ0232.2-4420	2230 ± 141	1380 ± 71	0.123 ± 0.013	1798 ± 167	1152 ± 137	0.178 ± 0.032
ZW3146	1875 ± 49	1206 ± 26	0.159 ± 0.010	2040 ± 77	1293 ± 22	0.135 ± 0.005
RXCJ0043.4-2037	1604 ± 157	1068 ± 82	0.176 ± 0.032	1472 ± 95	982 ± 133	0.199 ± 0.033
RXCJ0516.7-5430	2029 ± 246	1273 ± 114	0.127 ± 0.022	1767 ± 112	1135 ± 57	0.157 ± 0.013
RXCJ1131.9-1955	2121 ± 206	1325 ± 93	0.155 ± 0.023	2513 ± 271	1475 ± 97	0.120 ± 0.015

Notes. These estimates refer to the mass models obtained with two different methods (see Table 2) and are evaluated at the overdensities determined from the *total* (i.e. dark+gas) mass profiles. All the quoted errors are at 1σ level.

Table 4. Median deviations measured in the distribution of c_{200} , M_{DM} and f_{gas} .

Dataset	$(\hat{c}_{200} - c_{200})/c_{200}$	$(\hat{M}_{\text{DM}} - M_{\text{DM}})/M_{\text{DM}}$	$(\hat{f}_{\text{gas}} - f_{\text{gas}})/f_{\text{gas}}$
<i>Method 2</i>	-0.013	+0.008	+0.036
M2	+0.010	-0.017	+0.009
$T_{3\text{D}}$	-0.048	-0.036	+0.024
fit n_{gas}	+0.001	+0.011	+0.000
P_{out}	-0.011	+0.030	-0.014
at R_{200}	(-0.048, +0.010)	(-0.036, +0.030)	(-0.014, +0.036)
<i>Method 2</i>	-	-0.015	+0.035
M2	-	-0.018	+0.010
$T_{3\text{D}}$	-	-0.046	+0.025
fit n_{gas}	-	+0.012	-0.008
P_{out}	-	+0.028	-0.013
at R_{500}	-	(-0.046, +0.028)	(-0.013, +0.035)
<i>Method 2</i>	-	-0.073	+0.032
M2	-	-0.013	+0.008
$T_{3\text{D}}$	-	-0.059	+0.028
fit n_{gas}	-	+0.004	+0.000
P_{out}	-	+0.020	-0.009
at R_{2500}	-	(-0.073, +0.020)	(-0.009, +0.032)

Notes. The deviations are measured with respect to the estimates obtained from the combined $M1+M2$ profile with the *Method 1* for the whole sample of 44 clusters. Dataset: (*Method 2*) *Method 2* is used for mass reconstruction; (M2) only the $T(r)$ profile from M2 is used; ($T_{3\text{D}}$) the deprojected spectral measurements of $T(r)$ are used in *Method 1* instead of the projected estimates of T_{model} (see Sect. 3); (fit n_{gas}) a model fitted to the gas density profile is used in *Method 1*; (P_{out}) the outer value of the pressure is not fixed.

Table 5. Best-fit values of the $c_{200} - M_{200}$ relation.

Dataset	c_{15}	A	B	$\sigma_{\log_{10} c}$
All objects (44 clusters)				
<i>Method 1 - Weighted Mean</i>	$3.60^{+0.05}_{-0.05}$	0.556 ± 0.006	-0.1	0.193/0.116
<i>Method 1 - FITEXY</i>	3.62 ± 0.07	0.558 ± 0.008	-0.451 ± 0.023	0.135/0.116
<i>Method 1 - BCES</i>	3.78 ± 0.18	0.577 ± 0.021	-0.544 ± 0.071	0.132/0.116
<i>Method 1 - LINMIX</i>	3.79 ± 0.21	0.579 ± 0.025	-0.444 ± 0.077	0.132/0.116
<i>Method 2 - Weighted Mean</i>	$3.42^{+0.03}_{-0.03}$	0.534 ± 0.004	-0.1	0.203/0.119
<i>Method 2 - FITEXY</i>	3.21 ± 0.05	0.507 ± 0.006	-0.466 ± 0.015	0.146/0.119
<i>Method 2 - BCES</i>	3.51 ± 0.16	0.545 ± 0.020	-0.612 ± 0.084	0.133/0.119
<i>Method 2 - LINMIX</i>	3.72 ± 0.20	0.571 ± 0.024	-0.493 ± 0.067	0.131/0.119
Selected objects (26 clusters)				
<i>Method 1 - Weighted Mean</i>	$4.61^{+0.09}_{-0.09}$	0.664 ± 0.008	-0.1	0.165/0.092
<i>Method 1 - FITEXY</i>	4.06 ± 0.17	0.608 ± 0.018	-0.321 ± 0.050	0.143/0.092
<i>Method 1 - BCES</i>	3.84 ± 0.38	0.584 ± 0.043	-0.586 ± 0.116	0.138/0.092
<i>Method 1 - LINMIX</i>	4.24 ± 0.47	0.628 ± 0.048	-0.370 ± 0.125	0.132/0.092
<i>Method 2 - Weighted Mean</i>	$4.00^{+0.05}_{-0.05}$	0.602 ± 0.005	-0.1	0.181/0.079
<i>Method 2 - FITEXY</i>	2.87 ± 0.13	0.458 ± 0.020	-0.576 ± 0.063	0.169/0.079
<i>Method 2 - BCES</i>	3.18 ± 0.57	0.502 ± 0.078	-0.782 ± 0.259	0.150/0.079
<i>Method 2 - LINMIX</i>	3.93 ± 0.45	0.594 ± 0.050	-0.438 ± 0.131	0.130/0.079
only LEC objects (11 clusters)				
<i>Method 1 - Weighted Mean</i>	$4.14^{+0.09}_{-0.09}$	0.617 ± 0.009	-0.1	0.091/0.033
<i>Method 1 - FITEXY</i>	3.68 ± 0.15	0.565 ± 0.017	-0.297 ± 0.051	0.081/0.033
<i>Method 1 - BCES</i>	3.27 ± 0.52	0.514 ± 0.070	-0.472 ± 0.229	0.093/0.033
<i>Method 1 - LINMIX</i>	3.75 ± 0.45	0.574 ± 0.052	-0.279 ± 0.150	0.081/0.033
<i>Method 2 - Weighted Mean</i>	$3.81^{+0.05}_{-0.05}$	0.581 ± 0.005	-0.1	0.096/0.046
<i>Method 2 - FITEXY</i>	3.13 ± 0.11	0.496 ± 0.015	-0.376 ± 0.054	0.080/0.046
<i>Method 2 - BCES</i>	3.21 ± 0.75	0.506 ± 0.102	-0.450 ± 0.303	0.074/0.046
<i>Method 2 - LINMIX</i>	3.39 ± 0.36	0.530 ± 0.046	-0.377 ± 0.133	0.071/0.046
Simulations				
B01	4.29	0.632	-0.102	
D04	4.01	0.603	-0.130	
S06 – all, relaxed	4.64, 4.86	0.667, 0.687	$-0.120, -0.160$	
N07 – all, relaxed	3.77, 4.33	0.576, 0.636	$-0.110, -0.100$	
M08 / WMAP-1 – all, relaxed	3.47, 4.18	0.540, 0.621	$-0.119, -0.104$	
M08 / WMAP-3 – all, relaxed	2.94, 3.41	0.469, 0.533	$-0.088, -0.083$	
M08 / WMAP-5 – all, relaxed	2.98, 3.56	0.474, 0.551	$-0.110, -0.098$	

Notes. The best-fit values refer to equation 5 and are obtained by using (i) the linear least-squares fitting with errors in both variables (*FITEXY*), (ii) the linear regression method *BCES*, (iii) a Bayesian linear regression method (*LINMIX*). In the last column, the total ($\sigma_{\text{tot}} = \sum_i^N (y_i - A - Bx_i)^2/N$) and statistical ($\sigma_{\text{stat}} = \sum_i^N \epsilon_{y_i}^2/N$) scatters are quoted, where $y_i = \log_{10}(c_{200}(1+z))$, $x_i = \log_{10} M_{200}$, ϵ_{y_i} is the statistical error on y_i and N is the number of objects.

Table 6. Cosmological constraints on σ_8 and Ω_m .

Model	N data	γ	Γ	χ_c^2	σ_8	Ω_m adding f_{gas}	χ_{tot}^2
E01	26	0.596 ± 0.030	0.449 ± 0.012	33.4	$1.039^{+0.124}_{-0.106}$	$0.25^{+0.01}_{-0.01}$	79.3
(LEC) E01	11	0.558 ± 0.042	0.388 ± 0.018	8.3	$0.825^{+0.114}_{-0.083}$	$0.26^{+0.02}_{-0.01}$	38.3
(all) E01	44	0.569 ± 0.026	0.408 ± 0.012	64.0	$0.850^{+0.087}_{-0.056}$	$0.28^{+0.01}_{-0.01}$	184.0
B01+M08	26	0.668 ± 0.040	0.547 ± 0.014	33.4	$1.260^{+0.040}_{-0.076}$	$0.25^{+0.01}_{-0.01}$	79.1
NFW	26	0.718 ± 0.086	0.344 ± 0.036	35.4	$0.940^{+0.252}_{-0.150}$	$0.25^{+0.01}_{-0.01}$	81.8
E01 (b_c)	26	0.574 ± 0.032	0.418 ± 0.014	36.8	$0.939^{+0.108}_{-0.082}$	$0.25^{+0.01}_{-0.01}$	82.7
E01 (b_M)	26	0.591 ± 0.030	0.458 ± 0.012	33.3	$1.003^{+0.145}_{-0.089}$	$0.26^{+0.02}_{-0.01}$	79.5
E01 (b_c, b_M)	26	0.576 ± 0.032	0.423 ± 0.014	36.8	$0.936^{+0.102}_{-0.109}$	$0.26^{+0.02}_{-0.01}$	82.9
E01 (M_{tot})	26	0.588 ± 0.030	0.441 ± 0.012	28.7	$1.006^{+0.116}_{-0.081}$	$0.25^{+0.01}_{-0.01}$	74.9

Notes. These cosmological constraints are obtained from equations 6 and 7 corresponding to the confidence contours shown in Fig. 7. To represent the observed degeneracy, we quote the best-fit values of the power-law $\sigma_8 \Omega_m^\gamma = \Gamma$. Errors at 2σ (95.4%) level of confidence are indicated.

Table B.1. Results of the 10,000 MC runs of the $c - M$ relation fitted using the expression in equation 5.

Model	N obj	mean (rms) A	mean (rms) B	$B_{\text{obs}} \pm \sigma$	$P_{1\sigma}(B_{\text{obs}})$	$P_{3\sigma}(B_{\text{obs}})$
N07	44	0.585(0.034)	-0.140(0.106)	-0.451 ± 0.023	0.5	1.5
N07	26	0.583(0.047)	-0.130(0.136)	-0.321 ± 0.050	14.5	38.2
N07	11	0.570(0.051)	-0.134(0.153)	-0.297 ± 0.051	23.4	47.4
M08 / WMAP-1	44	0.610(0.041)	-0.095(0.135)	-0.451 ± 0.023	0.8	1.8
M08 / WMAP-1	26	0.591(0.057)	-0.154(0.175)	-0.321 ± 0.050	24.6	46.1
M08 / WMAP-1	11	0.611(0.067)	-0.140(0.206)	-0.297 ± 0.051	29.9	49.3
M08 / WMAP-3	44	0.524(0.040)	-0.073(0.130)	-0.451 ± 0.023	0.4	0.9
M08 / WMAP-3	26	0.510(0.056)	-0.118(0.170)	-0.321 ± 0.050	18.0	37.7
M08 / WMAP-3	11	0.526(0.065)	-0.107(0.200)	-0.297 ± 0.051	23.6	42.6
M08 / WMAP-5	44	0.541(0.039)	-0.087(0.125)	-0.451 ± 0.023	0.4	1.1
M08 / WMAP-5	26	0.525(0.054)	-0.139(0.162)	-0.321 ± 0.050	20.5	41.9
M08 / WMAP-5	11	0.544(0.062)	-0.125(0.189)	-0.297 ± 0.051	26.0	45.9

Notes. B_{obs} is the best-fit result quoted in Table 5. $P_{1\sigma}(B_{\text{obs}})$ and $P_{3\sigma}(B_{\text{obs}})$ indicate the percentage of MC runs that provides an estimate of B lower than $B_{\text{obs}} + 1\sigma$ and $B_{\text{obs}} + 3\sigma$, respectively.